Global patterns of Joule heating in the high-latitude ionosphere

X. X. Zhang,[1,2] C. Wang,[1] T. Chen,[1] Y. L. Wang,[3] A. Tan,[4] T. S. Wu,[5]
G. A. Germany,[5] and W. Wang[6]

Received 8 May 2005; revised 30 August 2005; accepted 29 September 2005; published 9 December 2005.

[1] A compiled empirical global Joule heating (CEJH) model is described in this study. This model can be used to study Joule heating patterns, Joule heating power, potential drop, and polar potential size in the high-latitude ionosphere and thermosphere, and their variations with solar wind conditions, geomagnetic activities, the solar EUV radiation, and the neutral wind. It is shown that the interplanetary magnetic field (IMF) orientation and its magnitude, the solar wind speed, *AL* index, geomagnetic K_p index, and solar radio flux $F_{10.7}$ index are important parameters that control Joule heating patterns, Joule heating power, potential drop, and polar potential size. Other parameters, such as the solar wind number density (N_{sw}) and Earth's dipole tilt, do not significantly affect these quantities. It is also shown that the neutral wind can increase or reduce the Joule heating production, and its effectiveness mainly depends on the IMF orientation and its magnitude, the solar wind speed, *AL* index, K_p index, and $F_{10.7}$ index. Our results indicate that for less disturbed solar wind conditions, the increase or reduction of the neutral wind contribution to the Joule heating is not significant compared to the convection Joule heating, whereas under extreme solar wind conditions, the neutral wind can significantly contribute to the Joule heating. Application of the CEJH model to the 16 July 2000 storm implies that the model outputs are basically consistent with the results from the AMIE mapping procedure. The CEJH model can be used to examine large-scale energy deposition during disturbed solar wind conditions and to study the dependence of the hemispheric Joule heating on the level of geomagnetic activities and the intensity of solar EUV radiation. This investigation enables us to predict global Joule heating patterns for other models in the high-latitude ionosphere and thermosphere in the sense of space weather forecasting.

Citation: Zhang, X. X., C. Wang, T. Chen, Y. L. Wang, A. Tan, T. S. Wu, G. A. Germany, and W. Wang (2005), Global patterns of Joule heating in the high-latitude ionosphere, *J. Geophys. Res.*, *110*, A12208, doi:10.1029/2005JA011222.

1. Introduction

[2] Joule heating in the high-latitude ionosphere and thermosphere is an important factor for several critical areas in space weather study, including satellite drag, position control, orbital insertion, and lifetime. The Joule heating has a much more significant effect upon the entire thermosphere than the particle precipitation does, and it affects the dynamics of the thermosphere, including the wind, temperature, composition, and density profiles. Therefore it is of critical importance to fully understand the basic properties of Joule heating, as well as its dependence on various solar wind, geomagnetic activity, and neutral wind conditions.

[3] Several studies have investigated height-integrated Joule heating in the high-latitude ionosphere using data from ground radar and low-altitude satellites or based on empirical models. *Foster et al.* [1983] used AE-C satellite data to statistically study the hemispheric Joule heating power as a function of K_p index, and they found that the hemispheric Joule heating power increases with K_p index. *Ahn et al.* [1983] studied the Joule heating rate as a function of geomagnetic indices *AE* and *AL* using limited Chatanika radar data, and they found that Joule heating rate increases with *AE* and *AL* indices. *Gary et al.* [1994] statistically investigated Joule heating distribution using DE-2 data during solar maximum. They found that the Poynting flux flowing into the ionosphere dominates over Joule heating dissipation, and Joule heating distributes along the dawn-dusk direction during summer and winter and the noon-midnight direction near the equinoxes. *Lu et al.* [1995]

[1]Key Laboratory of Space Weather, Center for Space Science and Applied Research, Chinese Academy of Sciences, Beijing, China.
[2]Now at Physics Department, Auburn University, Auburn, Alabama, USA.
[3]Space Science and Applications, Los Alamos National Laboratory, Los Alamos, New Mexico, USA.
[4]Physics Department, Alabama A. & M. University, Normal, Alabama, USA.
[5]Center for Space Plasma and Aeronomic Research, University of Alabama in Huntsville, Huntsville, Alabama, USA.
[6]High Altitude Observatory, National Center for Atmospheric Research, Boulder, Colorado, USA.

0148-0227/05/2005JA011222

found a good correlation between *AE* index and the hemispheric Joule heating rate based on a comprehensive data set from ground- and space-based measurements. Later, polar cap (*PC*) index was proposed as a proxy for Joule heating power obtained from the Assimilative Mapping of Ionospheric Electrodynamics (AMIE) procedure [*Chun et al.*, 1999]. The AMIE procedure [*Richmond and Kamide*, 1988] provides a global, quantitative estimation of Joule heating under given solar wind and geomagnetic conditions by combining various ground- and space-based measurements. *Fujii et al.* [1999] found that the Joule heating power has a positive correlation with K_p index using European Incoherent Scatter Common Program mode I data. A fair correlation between the hemispheric auroral power and *PC* index was determined based on Polar satellite data, and the best correlation of them was also found in the predawn and postdusk sectors [*Liou et al.*, 2003]. The Joule heating power calculated from a global MHD simulation [*Palmroth et al.*, 2004] was found to be much smaller than the estimated value given by *Ahn et al.* [1983]. *Olsson et al.* [2004] statistically studied Joule heating with Poynting flux method based on Astrid-2/EMMA electric and magnetic field data during solar maximum, and they reported a fitted Joule heating power as a function of K_p index, *AE* index, the Akasofu ε parameter and the solar wind kinetic energy flux in given magnetic local time (MLT) and invariant latitude (ILAT) ranges. Their results are in good agreement with those of *Foster et al.* [1983] and *Ahn et al.* [1983] but larger than *Palmroth et al.* [2004] simulation values. *Baker et al.* [2004] found that Joule heating dominates in the evening sector auroral oval and also in the vicinity of the region-1 current based on SuperDARN measurements and TIMED spacecraft Global Ultraviolet Imager (GUVI) auroral images.

[4] Most of these Joule heating estimations and the cause-effect relationship in the high-latitude ionosphere and upper atmosphere have been studied only intermittently and locally with a limited context and spatial and temporal coverage. Furthermore, it is very difficult to continuously monitor the Joule heating variations that are associated with solar wind conditions and geomagnetic activities over the entire polar region. The Joule heating distribution, as an important input for the upper atmosphere, can have a significant impact on the structure of the thermosphere and ionosphere on both local and global scales. The global spatial and temporal distribution of Joule heating, its dependence on variable solar-interplanetary-magnetosphere conditions, and its impact on the thermosphere and ionosphere have not been well understood. Because of the importance of Joule heating and the difficulty of calculating it, it is of great interest to the space physics community to construct an empirical model which provides a quick and efficient way to evaluate global Joule heating input to the thermosphere.

[5] For this purpose, we construct a compiled empirical global Joule heating (CEJH) model based on the fact that its validity and effectiveness depend on the validity and effectiveness of its constructing models. As a first-order estimation, this model can be used to study the global distribution of Joule heating and capture its basic behavior under different solar wind and IMF parameters, geomagnetic activities, and solar EUV radiation conditions. In this paper, we first describe the approach to construct the CEJH model in section 2. In section 3, we study the dependence of Joule heating on solar wind and IMF conditions, K_p index and $F_{10.7}$ index, as well as the neutral wind. In section 4, we apply the CEJH model to the 16 July 2000 magnetic storm and compare the model outputs with the results obtained from AMIE. Finally, we discuss and summarize the main results of this study in section 5.

2. Compiled Empirical Global Joule Heating (CEJH) Model

[6] Assuming that Joule heating is uniformly deposited in a limited altitude range at a particular altitude, say, 130 km in the high-latitude ionosphere and upper atmosphere at which the maximum Joule heating occurs [*Deng et al.*, 1995], the height-integrated Joule heating rate Q_J at a location of interest can be expressed as

$$Q_J = (\mathbf{E} + \mathbf{U} \times \mathbf{B}) \bullet \Sigma \bullet (\mathbf{E} + \mathbf{U} \times \mathbf{B}), \tag{1}$$

where **E** is the ionospheric electric field, **B** is the magnetic field, **U** is the neutral wind velocity and $\boldsymbol{\Sigma}$ is the height-integrated conductivity tensor, and (**E** + **U** × **B**) is the electric field in the frame of the neutral wind. The altitude-adjusted corrected geomagnetic (AACGM) coordinate is adopted in our calculation of the height-integrated Joule heating rate within a spherical shell at a particular altitude. In the coordinate, r is the radial distance, θ is the corrected geomagnetic (CGM) latitude, and ϕ is the MLT. In this frame, the height-integrated conductivity tensor, $\boldsymbol{\Sigma}$, can be expressed as

$$\Sigma = \begin{bmatrix} \Sigma_{\theta\theta} & \Sigma_{\theta\phi} \\ \Sigma_{\phi\theta} & \Sigma_{\phi\phi} \end{bmatrix}, \tag{2}$$

whose components are given by

$$\begin{aligned} \Sigma_{\theta\theta} &= \Sigma_P / \sin^2 I, \\ \Sigma_{\theta\phi} &= -\Sigma_{\phi\theta} = \Sigma_H / \sin I, \\ \Sigma_{\phi\phi} &= \Sigma_P, \end{aligned}$$

where I is the inclination of the geomagnetic field **B**, Σ_P and Σ_H are the height-integrated Pedersen and Hall conductivities, respectively. Plugging **E** = (E_θ, E_ϕ), **B** = (B_r, B_θ, B_ϕ) and **U** = (U_r, U_θ, U_ϕ) into equation (1), we can get the height-integrated Joule heating rate Q_J in terms of convection heating rate, Q_C, and neutral wind heating rate, Q_W.

$$\begin{aligned} Q_J &= Q_C + Q_W, \\ Q_C &= \Sigma_{\theta\theta} E_\theta^2 + \Sigma_{\phi\phi} E_\phi^2, \\ Q_W &= \Sigma_{\theta\theta} \left[2E_\theta \left(U_\phi B_r - U_r B_\phi \right) + \left(U_\phi B_r - U_r B_\phi \right)^2 \right] \\ &\quad + \Sigma_{\phi\phi} \left[2E_\phi (U_r B_\theta - U_\theta B_r) + (U_r B_\theta - U_\theta B_r)^2 \right]. \end{aligned} \tag{3}$$

When the ion drift velocity, (**E** × **B**)/B^2, is much larger than the neutral wind velocity, U, or the effect of the neutral wind is negligible ($Q_W \approx 0$), equation (3) simply represents the convection Joule heating rate, Q_C. From equation (3), it is noted that Q_W depends not only on neutral wind speed and

direction but also on electric field, magnetic field and the Pedersen conductivity. *Lu et al.* [1995] pointed out that the neutral wind effect on Joule heating could be significant at low-altitude ionosphere and upper atmosphere. In order to capture the basic characteristics of the Joule heating, we construct the CEJH model based on currently most robust and popular empirical models, which are used to calculate electric field **E**, magnetic field **B**, the Pedersen conductivity Σ_P, and the neutral wind velocity **U**.

2.1. Electric Potential

[7] Several empirical models have been developed to describe the electric potential in the high-latitude ionosphere. These models can provide inputs for simulation and space weather prediction models to study the basic behavior of polar Joule heating. The *Heppner and Maynard* [1987] model is based on the electric field measurements obtained from DE-2 satellite, and it provides convection patterns with a limited coverage for different IMF conditions. Models developed by *Lu et al.* [1989], *Rich and Hairston* [1994], *Weimer* [1995], and *Ruohoniemi and Greenwald* [1996] provide the basic structure of the ionospheric convection with a wide variety of IMF orientations and seasonal effects. *Ridley et al.* [2000] presented an empirical model for ionospheric electric potential based on the results from AMIE and discussed the correlation of the electric potential with the IMF B_y and B_z components. The statistical models presented by *Boyle et al.* [1997], *Papitashvili et al.* [1994, 1999], *Weimer* [1995, 2001], and *Shepherd et al.* [2002] allow one to predict the electric potential pattern for any IMF orientation with more versatility than the previous models. It is noted that *Weimer* [2001] developed an improved model (noted as the Weimer 2K model) of the ionospheric electric potential for a wide variety of IMF orientations, solar wind conditions, Earth's dipole tilt, and *AL* index values. The previous empirical models (as cited above) do not consider effects associated with nightside processes influenced by substorm activities in the magnetotail, whereas the Weimer 2K model includes the substorm effect. In the CEJH model therefore we adopt the *Weimer* [2001] electric field model to calculate the ionospheric electric potential and evaluate the electric field. However, caution must be taken when using the results from the Weimer 2K model when its input parameters exceed the coverage of the original data set.

[8] The electric field **E** in the high-latitude ionosphere can be decomposed into a mean electric field $\mathbf{E}_0$ and the electric field variation $\delta\mathbf{E}$, that is, $\mathbf{E} = \mathbf{E}_0 + \delta\mathbf{E}$. The mean electric field $\mathbf{E}_0$ driven by solar wind/IMF conditions can be specified using one of the empirical models as we mentioned, such as the Weimer 2K model. It is suggested by a number of authors that $\delta\mathbf{E}$ in the high-latitude ionosphere has been shown to play a significant role in high-latitude energy dissipation including Joule heating, and neglecting it may cause calculation error of Joule heating on different temporal and spatial scales [*Heppner et al.*, 1993; *Papitashvili et al.*, 1994; *Codrescu et al.*, 1995, 2000; *Crowley and Hackert*, 2001; *Matsuo et al.*, 2003]. Nevertheless, as the first step to construct the CEJH model, we do not include this effect in our calculations because of the lack of available specification models for such effect. However, if a good model of high-latitude ionospheric electric field variations is available, it is easily plugged into the CEJH model.

[9] The polar cap ionosphere has been shown to be able to reconfigure promptly after the arrival of an IMF structure [*Weimer*, 2001]; therefore it is very important to determine the time shift between the variations of the upstream solar wind and IMF parameters and their associated changes of the high-latitude ionospheric electric fields. The method given by *Shepherd et al.* [2002] is used to determine the time shift: (1) The time shift, τ_{sw}, from the upstream solar wind observer (the satellite's Sun-Earth line position, X_{sc}; the x component of the solar wind velocity, V_{xsw}) to the bow shock; (2) The time delay, τ_{mp}, from the bow shock to the magnetopause using the average shocked solar wind velocity with a reduction factor of 8; and (3) The estimated time, τ_{Alfven} (=1–3 min), of Alfvénic perturbation propagating from the magnetopause to the high latitude ionosphere. The bow shock position, X_{bs}, and magnetopause position, X_{mp}, along the Sun-Earth line can be obtained from *Chao et al.* [2001] bow shock and magnetopause models. The total time shift, T_{shift}, can be written as

$$\begin{aligned} T_{shift} &= \tau_{sw} + \tau_{mp} + \tau_{Alfven}, \\ \tau_{sw} &= \frac{X_{sc} - X_{bs}}{|V_{xsw}|}, \\ \tau_{mp} &= \frac{X_{bs} - X_{mp}}{|V_{xsw}|} \times 8, \\ \tau_{Alfven} &= 2.0 \ \mathrm{min}. \end{aligned} \tag{4}$$

The uncertainty in the determination of the time shift may be greatly reduced by using appropriate techniques to calculate these three different time shifts and choosing accurate bow shock and magnetopause models. Thus a caution must be advised when using time shifts from these formulae when upstream solar wind/IMF conditions highly vary with time.

2.2. Magnetic Field

[10] In our calculations we use the International Geomagnetic Reference Field (IGRF) model and the Tsyganenko model, which include the contributions from the inner geomagnetic field and external magnetospheric sources: the ring current, magnetotail current system, magnetopause currents, and the large-scale system of field-aligned currents [*Tsyganenko*, 1989]. For the low-altitude ionosphere and upper atmosphere, the main part of the geomagnetic field comes from the IGRF model for the inner geomagnetic field and a minor correction is from the Tsyganenko model.

2.3. Pedersen Conductivity

[11] The ionospheric conductivities, including the Hall and Pedersen conductivities, have been considered as important quantities in the estimation of the Joule heating in the high-latitude ionosphere and upper atmosphere. Even though how the ionospheric currents affect the conductivities (and vice versa) is not well understood, it is commonly assumed that changes in the ionospheric conductivities are mainly controlled by the solar EUV radiation, of which $F_{10.7}$ is a proxy, and particle precipitation [*Aksnes et al.*, 2002; *Zhang et al.*, 2004]. Because of the importance of the ionospheric conductivities in the coupled magnetosphere-ionosphere-thermosphere system, a number of global em-

pirical and physical models of the ionospheric conductivities have been developed based on particle precipitation, solar radio flux, and geomagnetic variation [*Spiro et al.*, 1982; *Hardy et al.*, 1987; *Rich et al.*, 1987; *Germany et al.*, 1994; *Ahn et al.*, 1998; *Gjorloev and Hoffman*, 2000a, 2000b; *Semeter and Doe*, 2002; *Aksnes et al.*, 2002].

[12] Since ionospheric conductivities are not directly measured parameters, any empirical models to obtain these parameters must involve some assumptions. For simplicity, the empirical models of particle precipitation by *Hardy et al.* [1987] and solar radio flux by *Rich et al.* [1987] are used in the CEJH model. These two models are controlled by a number of input parameters including the geomagnetic latitude and longitude, $F_{10.7}$ index, the solar zenith angle, and K_p index. The conductivities due to electron precipitation may be significant relative to that from solar radio fluxes during solar maximum [*Hardy et al.*, 1987], even though the conductivities from the solar radio fluxes in dayside dominate in most times, over that from electron precipitation in nightside. In our calculation, the total Pedersen conductivity can be expressed as

$$\Sigma_p = \sqrt{\Sigma_p^2(precipitation) + \Sigma_p^2(solar)}, \tag{5}$$

where Σ_p (precipitation) is the precipitation produced conductivity obtained directly from the Hardy model [*Hardy et al.*, 1987], and Σ_p (solar) is the solar EUV produced conductivity calculated from the Rich model [*Rich et al.*, 1987] with the form

$$\Sigma_p(solar) = \frac{12.5\sqrt{F_{10.7}/180}\{0.06 + \exp[1.803\tanh(3.833\cos\chi) + 0.5\cos\chi - 2.332]\}}{\left[1 + 0.3\sin^2\lambda\right]\sqrt{1 - 0.99524\cos^2\lambda}},$$

$$\cos\chi = \cos(\phi_{sun} - \phi)\cos\lambda\cos\delta_{sun} + \sin\lambda\sin\delta_{sun},$$

where χ is the solar zenith angle, $\delta_{\rm sun}$ and $\phi_{\rm sun}$ are the geomagnetic latitude and longitude of the Earth's subsolar point, and λ and ϕ are the geomagnetic latitude and longitude of the location of interest.

[13] During substorms, the use of empirical model conductivities from particle precipitation could significantly affect the Joule heating rate and the distribution of Joule heating. The importance of conductivities produced by electron precipitation to the dynamics of the auroral oval depends on its magnitude relative to the conductivity produced by the solar radio flux. The Hardy model can be used to calculate the global patterns of the height-integrated conductivity produced by the auroral electron precipitation for seven levels of geomagnetic activity (parameterized by K_p). However, a major limitation of this conductivity is that it uses a 3-hour K_p index and cannot reflect processes of much shorter scales because it contains a mixture of all IMF orientations and substorm phases (the typical timescale of auroral disturbances is minutes). As a first-order approximation, it can be used to estimate the global ionospheric conductivities in the CEJH model. In addition, this model can be easily replaced in the compiled model when better precipitation conductivity models are available.

2.4. Neutral Wind

[14] Solar wind and IMF conditions determine the levels of geomagnetic activities. The geomagnetic activity in turn controls the strength of high-latitude electric field and the intensity of particle precipitation. Particle precipitation enhances ionospheric electron density and thus ionospheric conductance in the auroral region. There have been a few studies to relate Joule heating rate to geomagnetic activity indices based on radar and satellite observations as discussed in section 1. However, most of these studies do not include the effect of thermospheric neutral winds on the Joule heating rate due to the difficulty in measuring the neutral winds. Neutral winds of 200–400 m/s can significantly influence the total Joule heating rate [*Rich et al.*, 1987]. It has been shown that neutral winds play an important role in deciding both the strength and spatial distribution of Joule heating [*Lu et al.*, 1995; *Thayer et al.*, 1995; *Emery et al.*, 1999; *Wang et al.*, 2004]. It is thus crucial to include neutral winds in evaluating the impact of energy input (Joule heating) from the solar wind and the magnetosphere on global thermospheric and ionospheric structures [*Ridley et al.*, 2003; *Richmond et al.*, 2003].

[15] Global measurements of neutral winds are not available; thus an empirical model has to be used to calculate **U** and estimate Q_W. The Horizontal Wind Model (HWM93) is an empirical model which was developed based on MF/Meteor radar observations, rocket data, and CIRA86 data, and covers all altitudes ranging from the ground to the thermosphere [*Hedin et al.*, 1996]. In the CEJH model, we use the horizontal wind model to calculate the neutral winds with $F_{10.7}$, A_p and geographic location of interest as input parameters. We need to mention here that the assumption of uniform **U** in the vertical direction in equation (1) is some sort of questionable even though it is more reasonable for **E** and **B**. However, when Q_W is not significant compared to Q_C and only a thin shell layer is considered at a particular altitude [*Baker et al.*, 2004], as a first-order approximation to estimate the influence of the neutral winds, this assumption should be appropriate.

3. Dependence of Joule Heating on Various Parameters

[16] In this section we use the CEJH model as described in the previous section to study high-latitude Joule heating patterns under different solar wind and IMF conditions, geomagnetic indices, and solar radio fluxes, in order to reveal the basic properties of the Joule heating pattern and to investigate the dependence of Joule heating on these parameters. First, we study the dependence of the Joule heating pattern on solar wind conditions, geomagnetic indices, and solar radio fluxes in the absence of the neutral wind. Then we study the effect of the neutral wind on the Joule heating pattern and the dependence of the neutral wind effects on solar wind and IMF conditions, geomagnetic indices, and solar radio fluxes.

3.1. Dependence of Joule Heating on the IMF

[17] High-latitude Joule heating patterns obtained from the CEJH model for IMF clock angles increasing from

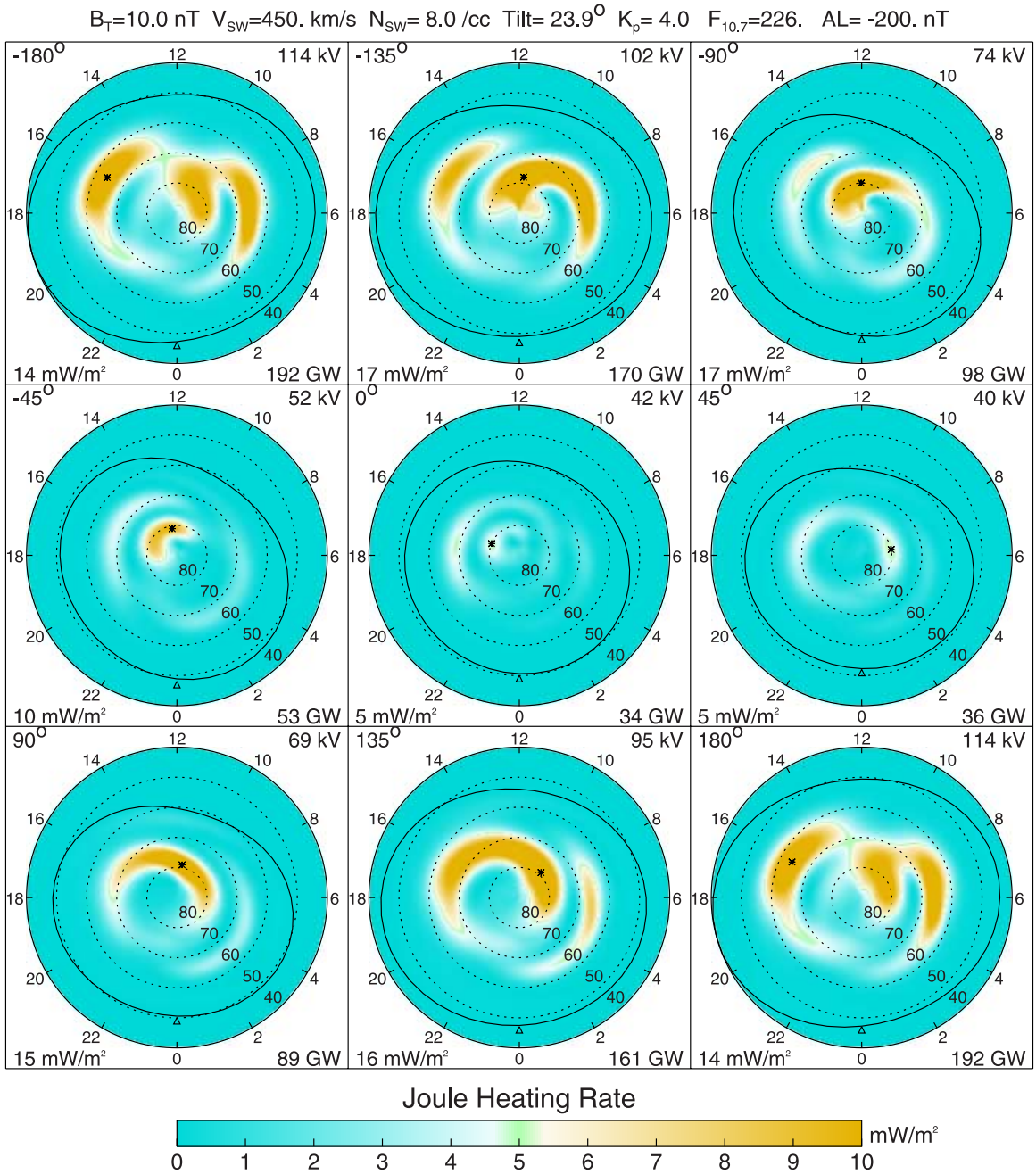

Figure 1. Joule heating patterns for different IMF clock angles from −180° to 180° for every 45° on 16 July 2000. All the other inputs are fixed with B_T = 10 nT, V_{sw} = 450 km/s, N_{sw} = 8 cm^{-3}, dipole tilt angle = 23.9°, K_p = 4.0, and $F_{10.7}$ = 226. Note that the IMF clock angle, the potential drop, the location of peak Joule heating rate (indicated with an asterisk in each box), and the total Joule heating power are shown in the upper left, upper right, lower left, and lower right corners of each box. The closed solid line in each circle shows the polar potential area.

−180° to 180° at 45° steps at 1200 UT on 16 July 2000 are shown in Figure 1 (this specific time is only used for calculating the Earth's dipole tilt and the neutral wind velocity in section 3.5). The IMF clock angle, atan(B_y/B_z), is defined as the angle, looking to the Earth from the Sun, clockwise/anticlockwise (positive/negative) from the Z axis in the GSM yz plane. All other inputs are fixed with IMF $B_T = \sqrt{B_y^2 + B_z^2}$ = 10 nT (B_x = 0.5 nT, not used in our calculation), the solar wind speed V_{sw} = 450 km/s, the solar wind number density N_{sw} = 8 cm^{-3}, the Earth's dipole tilt = 23.9° (positive for north magnetic pole toward the Sun), K_p = 4.0, and $F_{10.7}$ = 226. The IMF clock angle, the cross polar cap potential drop (potential drop), the peak Joule heating rate (indicated with an asterisk) and the total Joule heating power (integrated over hemisphere) are shown in the upper left, upper right, lower left, and lower right corners of each box. The closed black solid line in each plot shows the low-latitude boundary of the electric potential, below

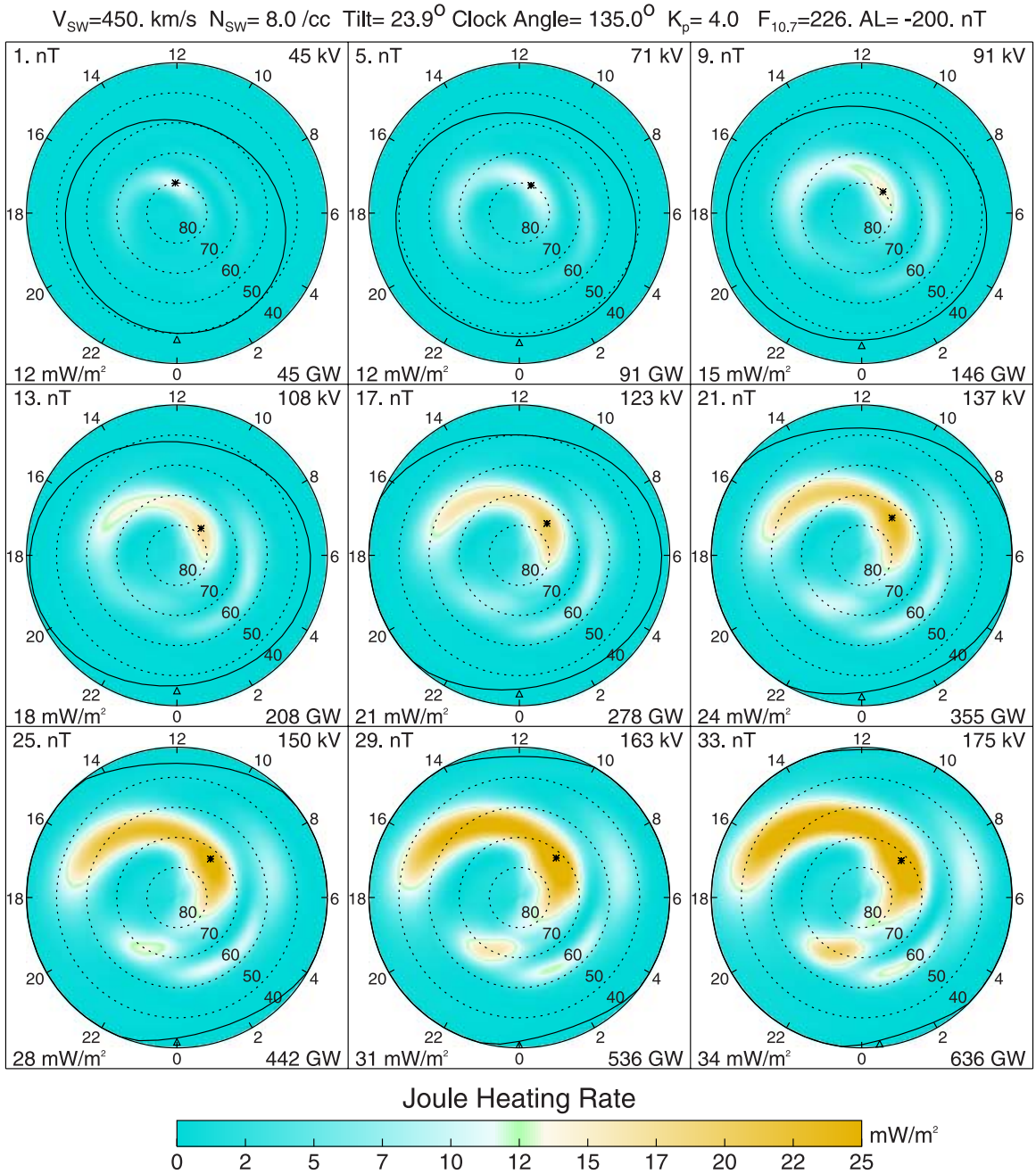

Figure 2. Dependence of Joule heating pattern on the magnitude of the IMF for a fixed clock angle of 135°. B_T is increased from 1 to 33 nT for every 4 nT and it is noted in the upper left of each box. All the other settings are the same as those in Figure 1.

which the magnetospheric imposed electric potential vanishes [*Weimer*, 2001]. In this paper the area encircled by this black solid line is defined as the polar potential area, where the electric potential is considered, and where the coupling between the magnetosphere and ionosphere occurs.

[18] In Figure 1, the IMF clock angle controls the Joule heating patterns. Northward IMF (zero clock angle) leads to a minimum Joule heating and the smallest polar potential size. Increasing the magnitude of the IMF clock angle results in an increase of Joule heating with different patterns. Positive and negative IMF clock angles with the same magnitude, such as 135° and −135°, produce roughly antisymmetric patterns but with some differences. Southward IMF generates the most Joule heating power, the largest potential drop and polar potential size. The boundary of the polar potential also moves to lower latitudes as the magnitude of the IMF clock angle increases. The more southward the IMF, the larger the polar potential size.

[19] Figure 2 shows the dependence of the Joule heating pattern on IMF B_T for a fixed IMF clock angle of 135°. With the increase of B_T, the potential drop increases as shown in the upper right corner of each box. Also, the Joule heating pattern expands to lower latitudes; the peak of the Joule heating rate moves to the dawn sector and the peak value also increases. Meanwhile, the Joule heating rate and the Joule heating power increase over the hemisphere as B_T

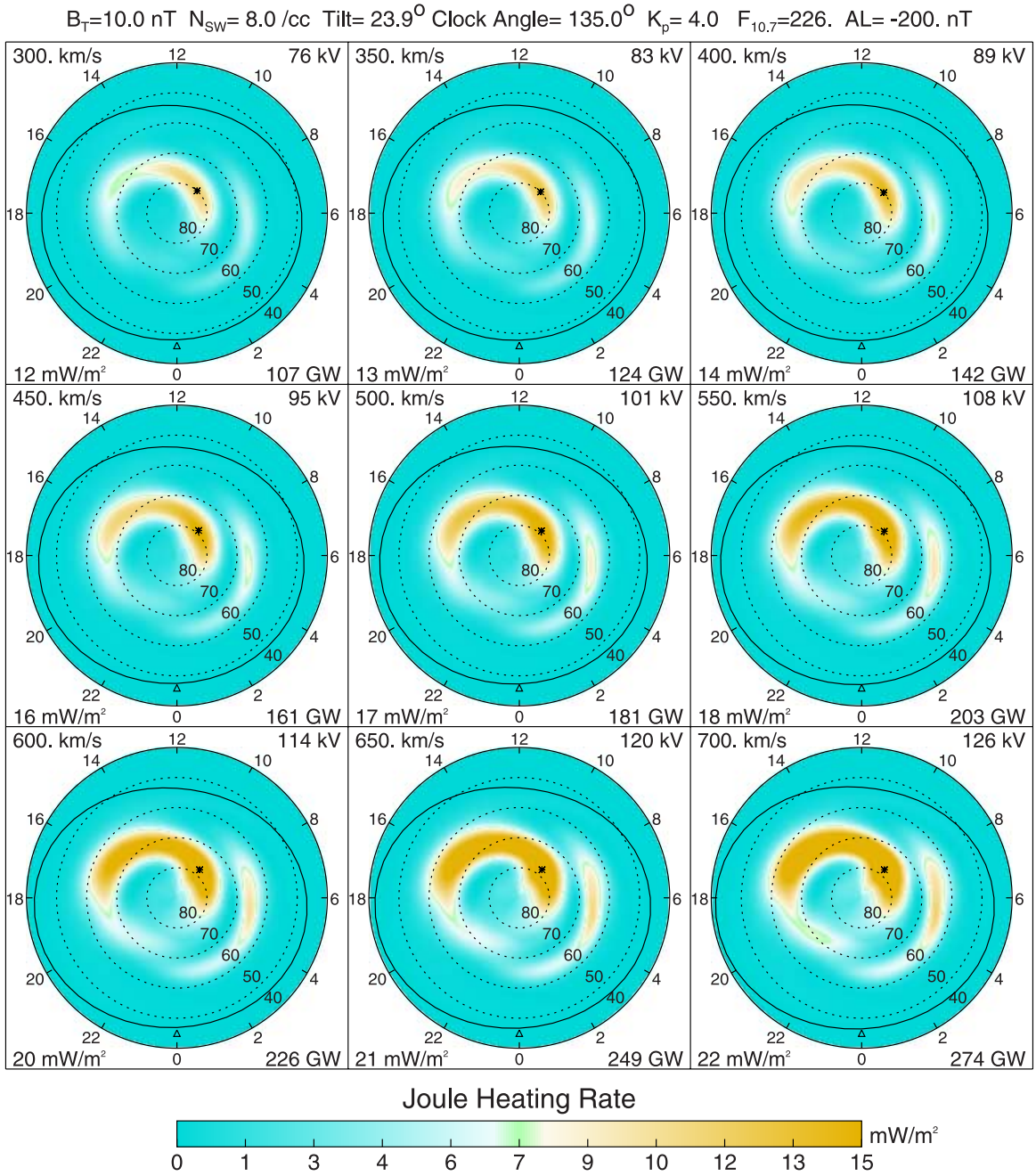

Figure 3. Dependence of the Joule heating pattern on the speed of the solar wind for a fixed IMF clock angle of 135°. V_{sw} is increased from 300 to 700 km/s for every 50 km/s and it is noted in the upper left of each box. All the other settings are the same as those in Figure 1.

increases. The nightside Joule heating rate becomes stronger with larger B_T. Under extreme solar wind conditions, such as those during the 16 July 2000 storm, the solar wind and IMF are highly disturbed as shown in Figure 13. It would be inferred that this highly disturbed strong IMF can produce complicated Joule heating patterns, high Joule heating rate, and large Joule heating power and polar potential size (see section 4).

3.2. Dependence of Joule Heating on V_{sw} and N_{sw}

[20] Figure 3 shows the Joule heating patterns with various solar wind speed from 300 to 700 km/s for every 50 km/s, Figure 4 shows the dependence of the Joule heating pattern on different solar wind density values from 1 to 17 cm^{-3} for every 2 cm^{-3}, both for a fixed IMF clock angle of 135°. The V_{sw} and N_{sw} values are noted in the upper left of each box of Figures 3 and 4, respectively. The other settings are the same as those in Figure 1.

[21] The solar wind dynamic pressure is one of the important factors in controlling the convection potential [*Weimer*, 2001]. It is shown in Figure 3 that increasing the solar wind speed can produce larger potential drop and enhance the convection electric field. Polar potential size is slightly increased as the solar wind speed increases. Also, increasing the solar wind speed results in an increase of the Joule heating rate and power. In contrast, increasing the

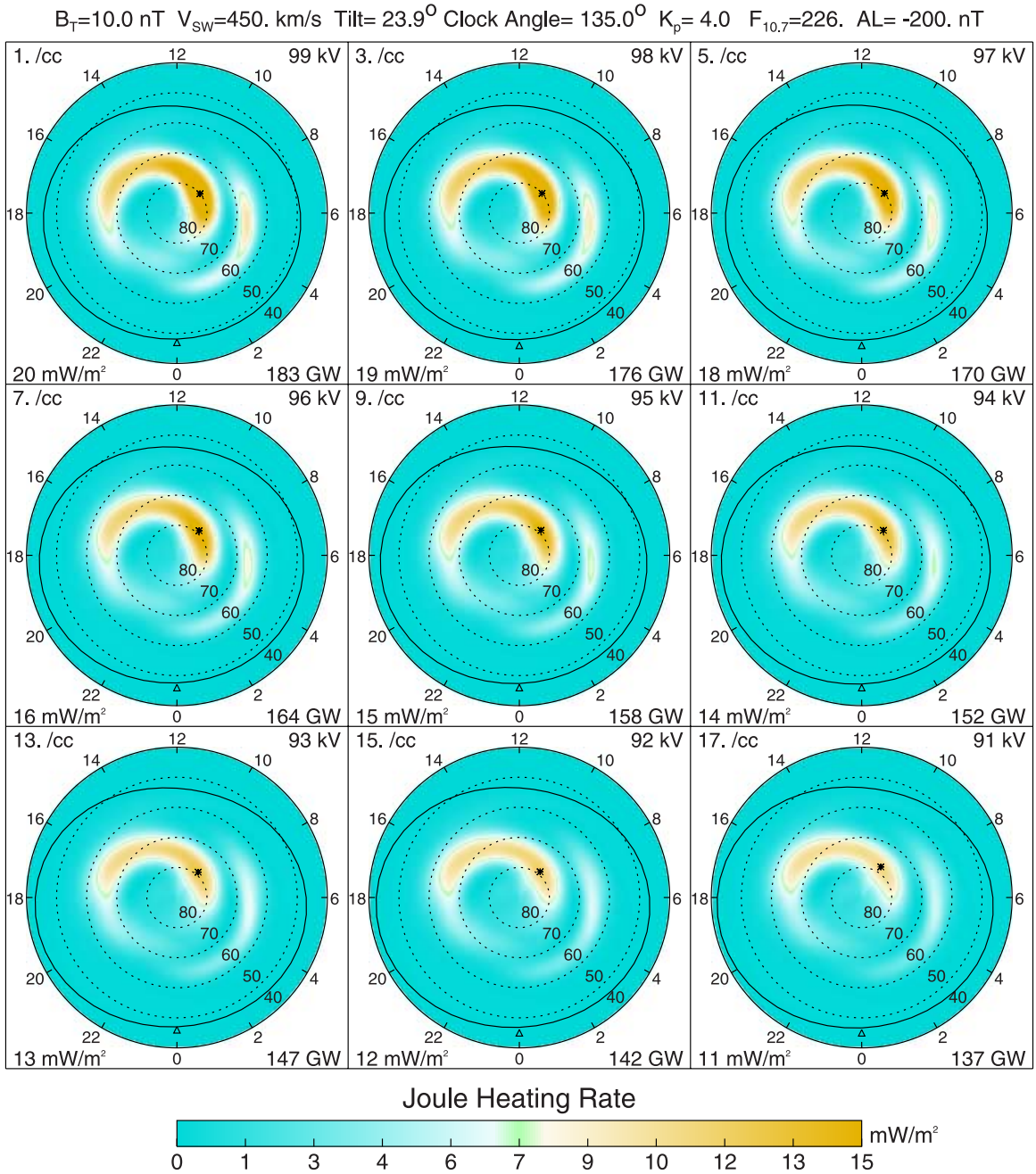

Figure 4. Dependence of the Joule heating pattern on the solar wind density for a fixed IMF clock angle of 135°. N_{sw} is increased from 1 to 17 cm^{-3} for every 2 cm^{-3} and it is noted in the upper left of each box. The other settings are the same as those in Figure 1.

solar wind number density does not produce more Joule heating as shown in Figure 4 because the potential drop does not increase. In both Figures 3 and 4, one can see that the Joule heating pattern does not change much with the increase of the solar wind speed and density. It can be seen that, however, the Joule heating rate peak value, the potential drop, and the Joule heating power increase by 10 mW/m^2, 50 kV, and 167 GW, respectively, and the polar potential area expands to lower latitudes, when the solar wind speed increases by 400 km/s. Whereas the Joule heating rate peak value, the potential drop and the Joule heating power decrease but the polar potential size slightly increases as the solar wind density increases. From Figure 13, the solar wind speed is much higher than the normal solar wind speed during this super storm; it is expected thus that this super fast solar wind could greatly enhance Joule heating (see section 4).

3.3. Dependence of Joule Heating on *AL* and K_p Indices

[22] It is known that the magnetospheric substorm (parameterized as the *AL* index) can significantly affect the cross polar potential pattern [*Weimer*, 2001]; therefore it should be an important factor to be considered in the calculation of the Joule heating. Figure 5 shows the depen-

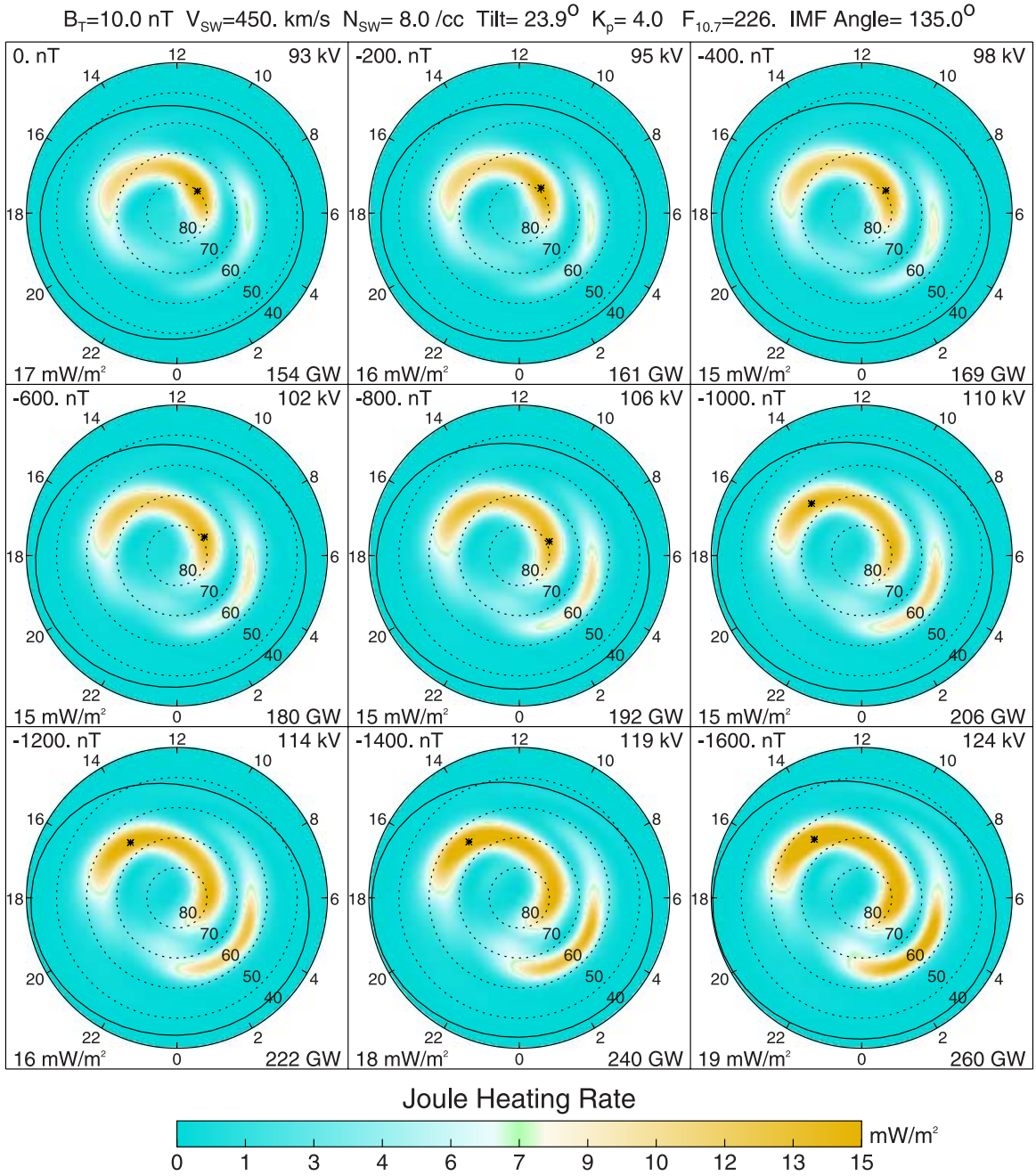

Figure 5. Dependence of the Joule heating pattern on *AL* index for a fixed IMF clock angle of 135°. The *AL* index is decreased from 0 nT to −1600 nT for every 200 nT and it is noted in the upper left of each box. All the other inputs are the same as those in Figure 1.

dence of the Joule heating pattern for a fixed IMF clock angle of 135° for various *AL* index values from 0 nT to −1600 nT for every 200 nT, while all the other inputs are the same as those in Figure 1. In Figure 5, one can see that the total Joule heating power, the potential drop, and the polar potential size increase as *AL* index increases. The Joule heating rate in the sector of the midnight-dawn intensifies with increasing *AL* index. The peak of the Joule heating rate shifts to the postnoon sector from the prenoon sector as *AL* index increases, but the peak Joule heating rate does not change much.

[23] K_p or A_p index indicates the disturbance level of geomagnetic activities in the polar region [*Hardy et al.*, 1987], and therefore it is another important parameter considered in the CEJH model. Figure 6 presents Joule heating patterns for a fixed IMF clock angle of 135° for various K_p index values from 1 to 9. The Joule heating power and nightside Joule heating rate increase as K_p index increases from 1 to 6. The Joule heating pattern does not change anymore when $K_p > 6$, because the Pedersen conductivity from *Hardy et al.* [1987] model does not change when $K_p > 6$. In Figure 6, the polar potential size and the potential drop do not change due to the absence of K_p index in the electric field model. The Joule heating in the sector of the midnight-dawn also intensifies with increasing K_p index (due to the increase of Pedersen conductivity).

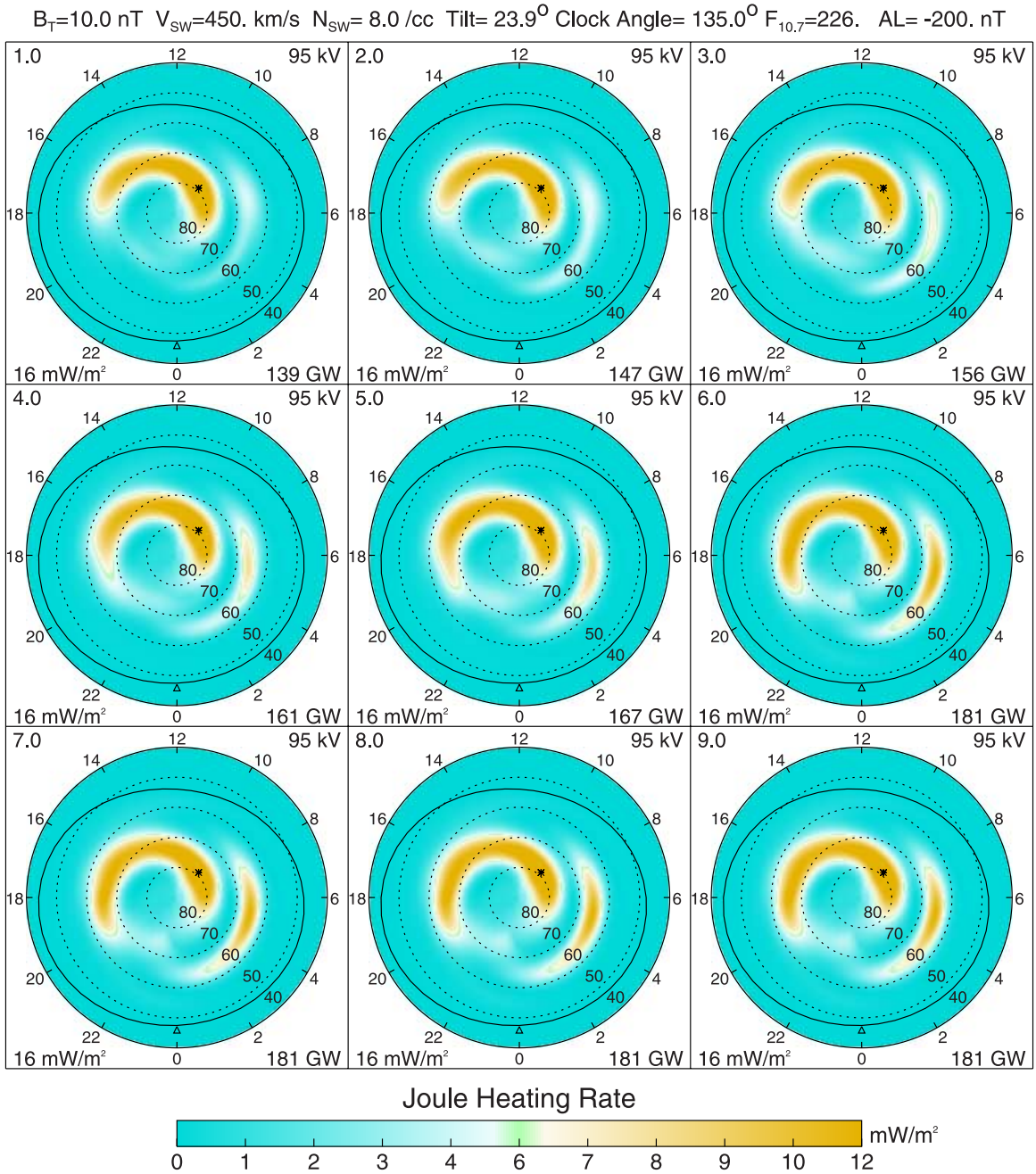

Figure 6. Dependence of the Joule heating pattern on K_p index for a fixed IMF clock angle of 135°. The K_p index is increased from 1 to 9 for every 1.0 and it is noted in the upper left of each box. All the other inputs are the same as those in Figure 1.

[24] It is noted that the AL, K_p, or A_p indices are not independent to each other. It should be of importance to find the relationships between them and upstream solar wind parameters in order to effectively estimate the Joule heating in the high-latitude ionosphere.

3.4. Dependence of Joule Heating on $F_{10.7}$ and the Earth's Dipole Tilt

[25] The Pedersen conductivity (see equation (5)) is a function of the solar zenith angle, the geomagnetic latitude and longitude of the Earth's subsolar point, as well as the geomagnetic latitude and longitude of the location of interest. Besides these parameters, it mainly depends on solar EUV radiation. Figure 7 shows Joule heating patterns for a fixed IMF clock angle of 135° with different solar radio flux $F_{10.7}$ index values from 60 to 300 for every 30. $F_{10.7}$ index value is noted in the upper left of each box and all the other settings are the same as those in Figure 1. It is shown that the Joule heating pattern does not change much, but the peak Joule heating rate enhances as $F_{10.7}$ index increases and the total Joule heating power also increases. Thus the intensification of the solar EUV radiation, indicated by $F_{10.7}$, can significantly increase the Joule heating over the global scales.

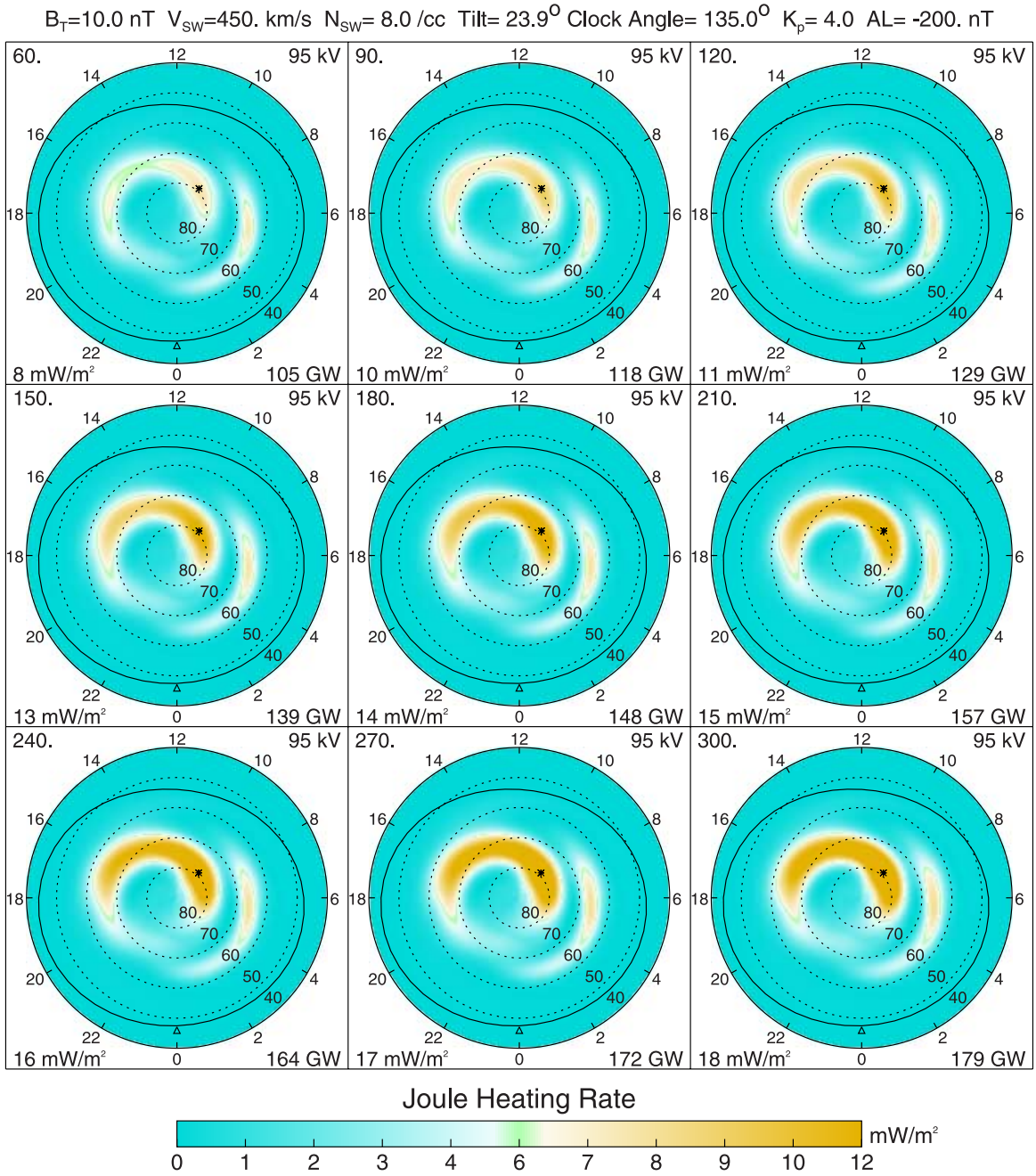

Figure 7. Dependence of the Joule heating pattern on the solar radio flux $F_{10.7}$ for a fixed IMF clock angle of 135°. $F_{10.7}$ index is increased from 60 to 300 for every 30 and it is noted in the upper left of each box. All the other settings are the same as those in Figure 1.

[26] Note that the potential drop is influenced by the dipole tilt angle and the IMF clock angle at which the potential drop peak location depends on the season or the dipole tilt angle [*Weimer*, 2001]. It is expected that the Earth's dipole tilt affects the Joule heating distribution. Figure 8 presents the dependence of the Joule heating pattern on the Earth's dipole tilt with a fixed IMF clock angle of 135° for different Earth's dipole tilt angles from 0° to 32° for every 4°. The global pattern of the Joule heating, the total Joule heating power, the potential drop, and the polar potential size do not change much as the tilt angle increases. From Figure 1 one can see that the Joule heating patterns for the same dipole tilt are different for different IMF clock angles. However, the Joule heating pattern does not change much with increasing dipole tilt for a fixed IMF clock angle.

3.5. Dependence of Joule Heating on the Neutral Wind

[27] From the term Q_W in equation (3), one can see that the effect of the neutral wind on the Joule heating depends on the Pedersen conductivity, electric field, geomagnetic field, and the neutral wind velocity at the high-latitude ionospheric *E* region heights. It is also noted that the geomagnetic field and the neutral wind distribution, as

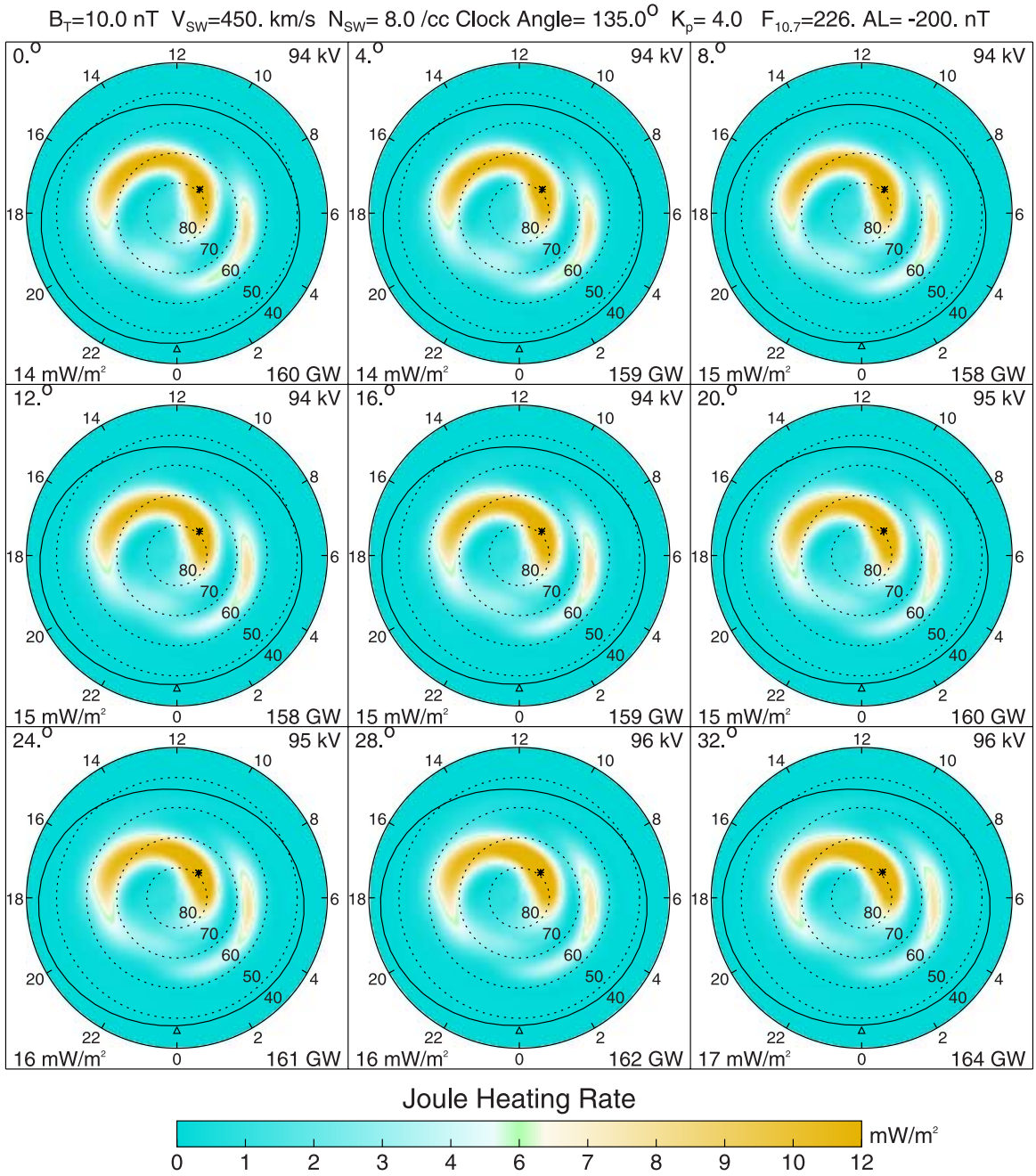

Figure 8. Dependence of the Joule heating pattern on the Earth's dipole tilt angle for a fixed IMF clock angle of 135°. The dipole tilt angle is increased from 0° to 32° for every 4° and it is noted in the upper left of each box. All the other settings are the same as those in Figure 1.

discussed in section 2, only depend on dipole tilt, K_p or A_p index, $F_{10.7}$ index, and the location of interest. In the following calculation, for simplicity, we only consider the term Q_w in equation (3) in this section, that is, the neutral wind contribution to the Joule heating.

[28] Figure 9 shows the Joule heating patterns for various IMF clock angles from −180° to 180° for every 45°. All the other inputs are the same as those in Figure 1. The IMF clock angle, the Joule heating power, the minimum and maximum Joule heating rates (indicated with asterisks and triangles) are shown in the upper left, upper right, lower left, and lower right corners of each box. The figure shows that there are several highs and lows in the Joule heating distributions with peak in the postnoon sector for all IMF clock angles except for the IMF clock angle of 90°. It is shown that the total Joule heating power and the Joule heating rate only from the neutral wind effect are quiet small compared with those in Figure 1. Since the neutral wind does not affect the potential drop as discussed in section 2, the potential drop and the polar potential size in Figure 9 are the same as those in Figure 1 for the corresponding IMF orientation. The neutral winds from HWM93 are the same for different IMF orientations, and the changes in the Joule heating thus come only from the potential drops. It is also noted from Figure 9 that the IMF orientation controls the Joule heating pattern, and the Joule heating rate and the

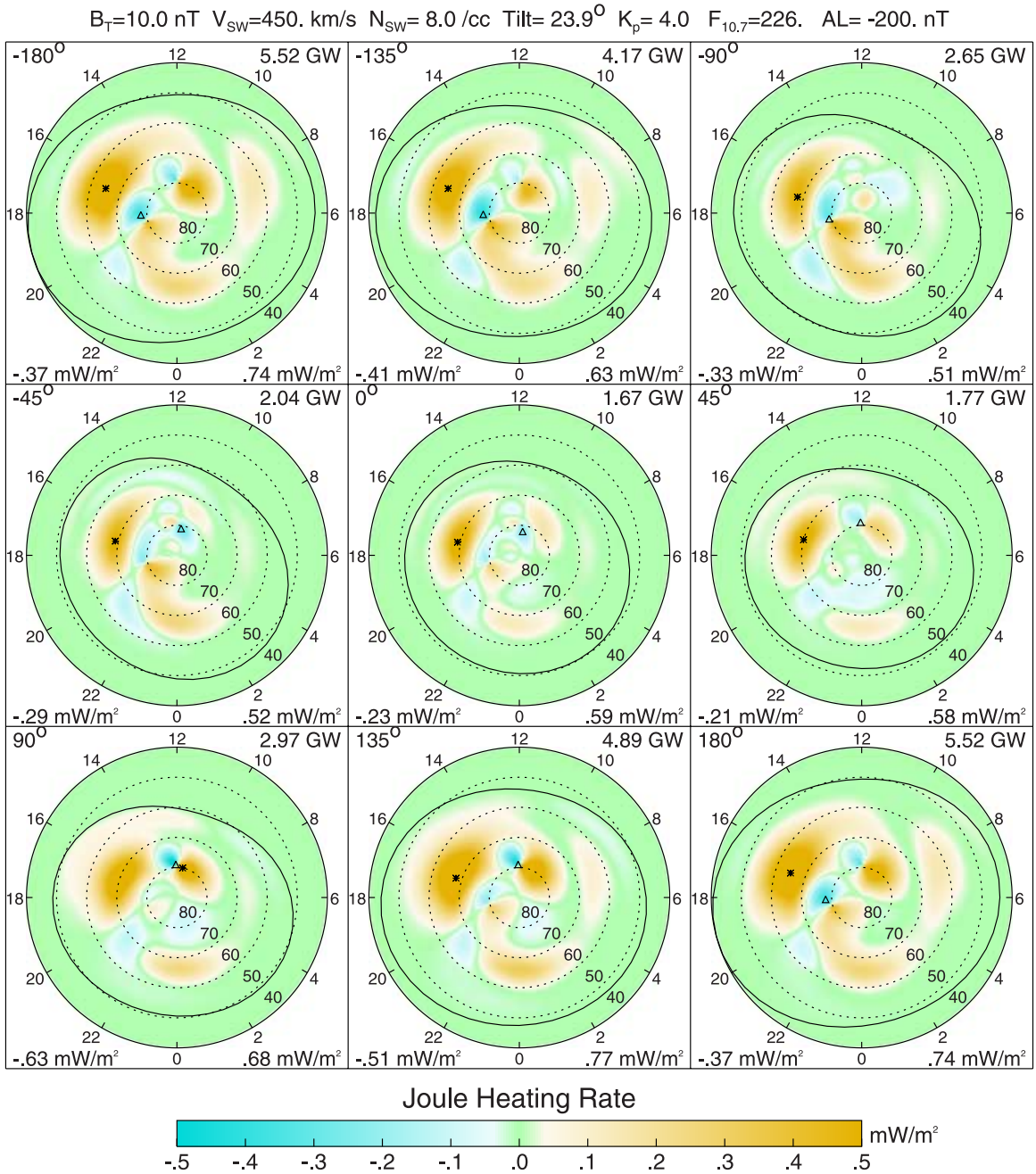

Figure 9. The Joule heating patterns (with only neutral wind effect) for various IMF clock angles from −180° to 180° for every 45°, which are noted in the upper left of each box. Asterisks and triangles indicate the locations of the maximum and minimum Joule heating rates in each box. All the other inputs are the same as those in Figure 1.

Joule heating power both increase as the magnitude of the IMF clock angle increases.

[29] *AL* index plays an important role in determining the polar potential pattern, and therefore it also affects the Joule heating rate, the Joule heating pattern, and the Joule heating power when the neutral wind distribution is given. Figure 10 shows the Joule heating patterns for a fixed IMF clock angle of 135°. *AL* index varies from 0 to −1600 nT for every 200 nT and it is noted in the upper left of each box. All the other inputs are the same as those in Figure 9. The figure shows that there are several highs and lows in the Joule heating distributions. The peak of the Joule heating rate stays in the dusk sector as the magnitude of *AL* increases. One can see that the Joule heating power increase when increasing the magnitude of *AL* index, but the Joule heating pattern does not change significantly and the polar potential size increases slightly. Therefore it can be inferred that an intense substorm (corresponding to a strong electric field) could enhance the neutral wind contribution to Joule heating and increase the total Joule heating power. We have noticed that it is not appropriate to set K_p or A_p index as a constant for neutral winds when the magnitude of *AL* index

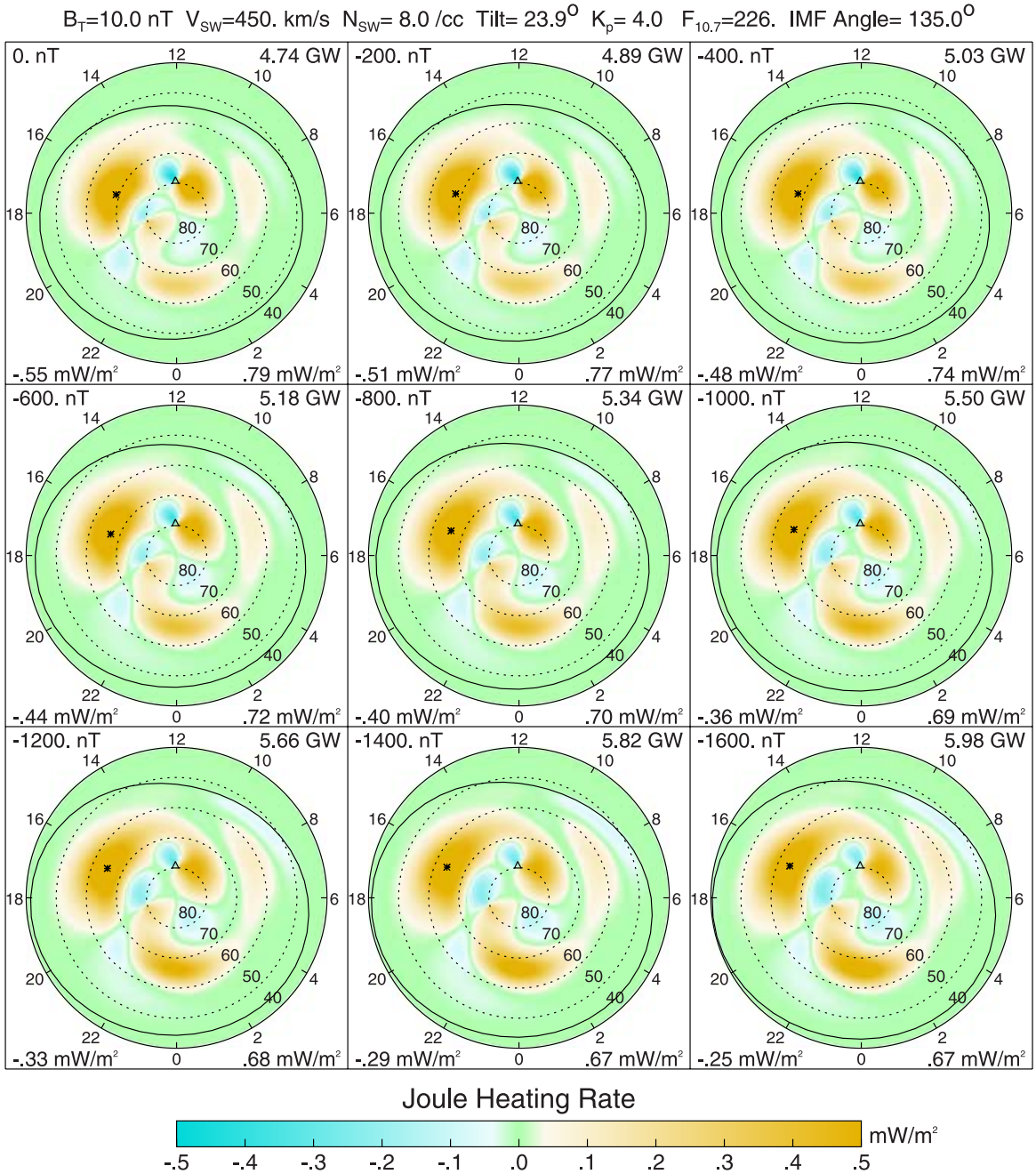

Figure 10. The Joule heating patterns (with only neutral wind effect) for a fixed IMF clock angle of 135° with different *AL* index from 0 to −1600 nT for every 200 nT which is noted in the upper left of each box. All the other inputs are the same as those in Figure 9.

increases. We will find the relation between K_p and *AL* indices in the future study.

[30] Given *AL* index and solar wind and IMF parameters, i.e., the electric potential pattern, K_p (or A_p) index and $F_{10.7}$ index are the main factors to control the neutral wind distribution. Figure 11 shows the dependence of the Joule heating pattern on K_p index. The maximum peak of the Joule heating rate shifts from prenoon to postnoon as K_p index increases, while the minimum peak stays in dayside. With the increase of K_p index, particle precipitation, the Pedersen conductivity and the neutral winds intensify, and the magnitude of the positive Joule heating rate exceeds that of the negative Joule heating rate. Thus the Joule heating power increases. It is also shown that the Joule heating patterns change significantly as K_p index increases. In contrast, the enhancement of the solar radio flux increases the total Joule heating power as shown in Figure 12. Figure 12 also shows that the Joule heating pattern does not change much for different $F_{10.7}$ index values. Also, the peaks of the Joule heating rate always stay in duskside when $F_{10.7}$ index increases.

[31] Given the electric potential pattern, K_p (or A_p) index and $F_{10.7}$ index control the neutral wind distribution, but the neutral wind speed from HWM93 is only several hundreds

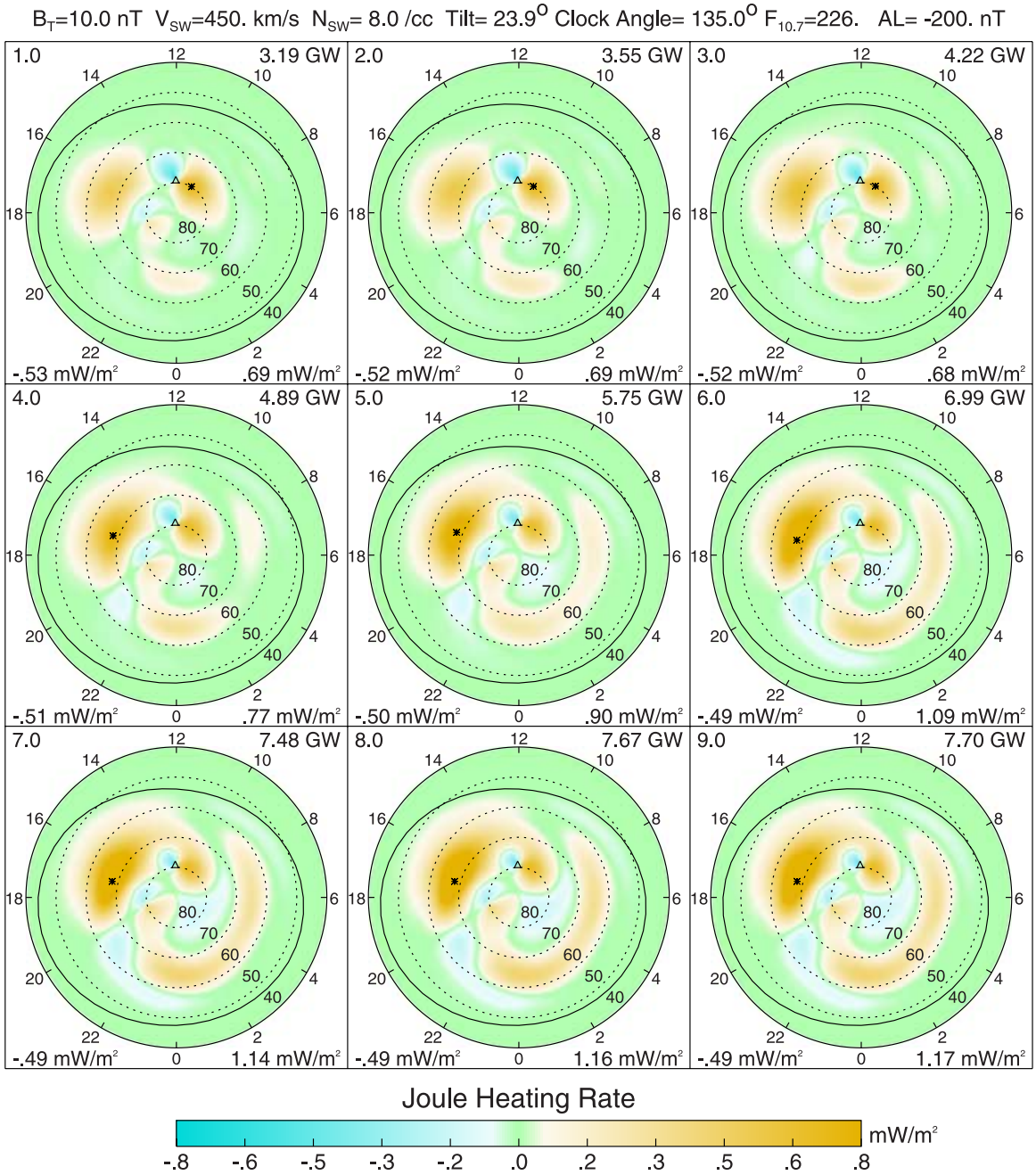

Figure 11. The Joule heating patterns (with only neutral wind effect) for a fixed IMF clock angle of 135° with various K_p index values from 1 to 9, which are noted in the upper left of each box. All the other inputs are the same as those in Figure 9.

m/s at low altitude (such as 130 km) over the polar region. Therefore from Figures 11 and 12, one can see that the neutral wind contribution to the Joule heating is not significant at low-altitude ionosphere and upper atmosphere compared with the convection Joule heating.

[32] A surprising finding from the above parametric studies is that Joule heating in the high-latitude ionosphere is stronger at the dayside than at the nightside. It is also found that there is a strong dawn-dusk Joule heating asymmetry over the nightside, with weaker Joule heating in the premidnight than the postmidnight sector. Since the Joule heating rate is proportional to the square of the electric field, it is expected that Joule heating is more closely related to the distribution of the ionospheric electric field. However, the different ionospheric conductivities may also have a strong influence on the distribution of Joule heating [*Lu et al.*, 2001]. The strong noon-midnight asymmetry of Joule heating distribution is mainly caused by the strong Pedersen conductivity in the dayside, whereas the dawn-dusk asymmetry of Joule heating is partially produced by the asymmetric Pedersen conductivity from the Hardy model [*Hardy et al.*, 1987] and is mainly produced by the weak electric fields in the premidnight region. The Hardy model provides two conductivity maxima in the nightside auroral oval: one

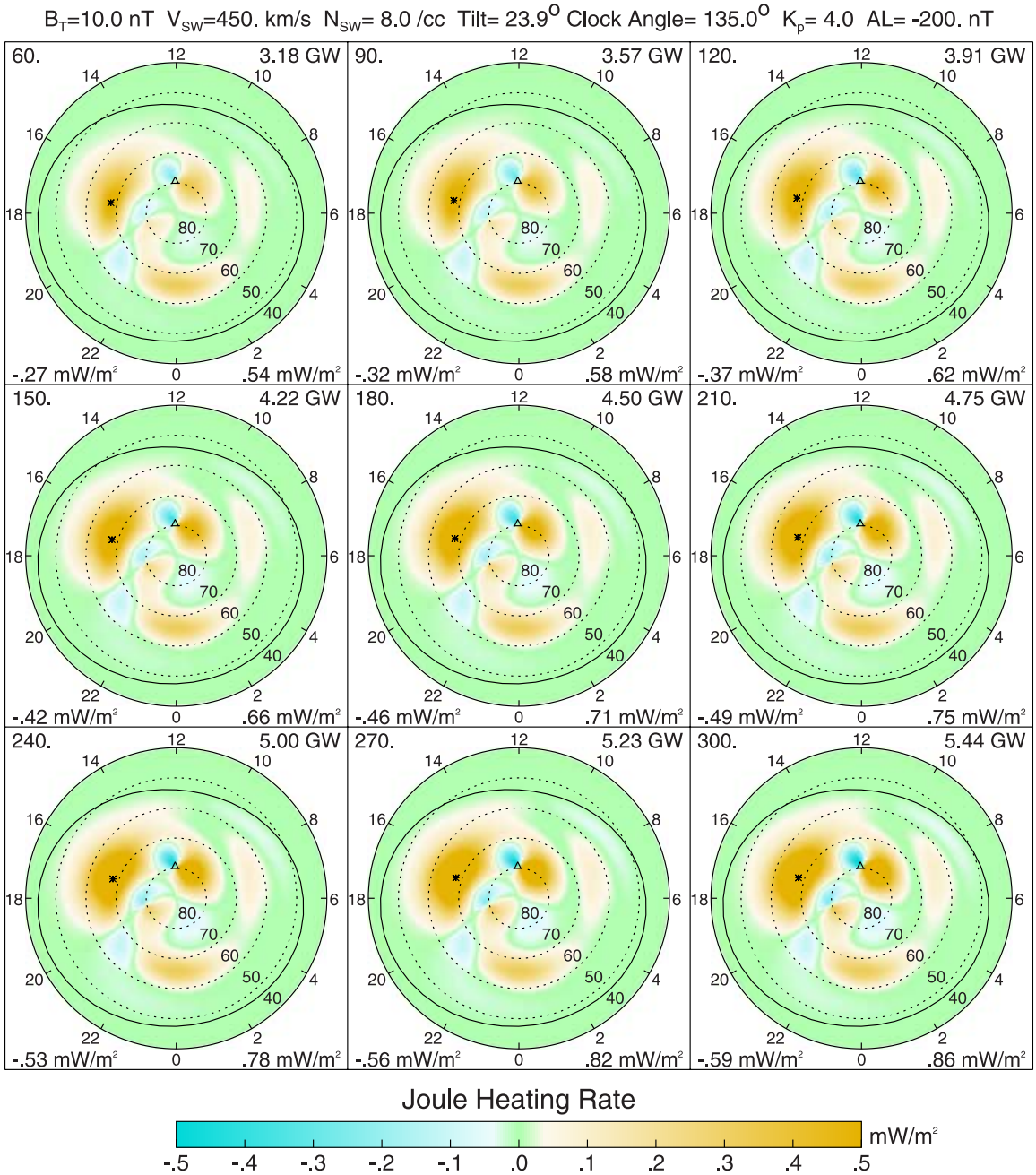

Figure 12. The Joule heating patterns (with only neutral wind effect) for a fixed IMF clock angle of 135° for different $F_{10.7}$ index values from 60 to 300 for every 30, which are noted in the upper left of each box. All the other inputs are the same as those in Figure 9.

near the midnight and the other in the postmidnight region. This characteristics of the Hardy model may be responsible for the lower Joule heating rate in the premidnight region, as clearly shown in Figure 6. The clockwise tilted electric potential distribution along the dawn-dusk can also produce weaker electric fields in the premidnight region, which can also result in weaker Joule heating in this region.

4. Application of the CEJH Model to the 16 July 2000 Storm

[33] In section 3 we have investigated the dependence of the Joule heating pattern, Joule heating power, potential drop, and polar potential size on some solar wind and IMF parameters, *AL*, K_p, and $F_{10.7}$ indices, as well as the neutral wind. In this section, we apply our compiled empirical model to the 16 July 2000 storm, which has been widely studied in geophysics community (*Solar Physics*, *204*, 2001), and then compare the outputs of our model with the results from AMIE.

[34] Figure 13 shows some time-shifted solar wind and IMF parameters, and *AL* and K_p indices on 16 July 2000. In this figure, the IMF, *AL*, and K_p are interpolated according to the solar wind plasma data with 5-min time resolution. The solar radio flux $F_{10.7}$ index is fixed at 226 for our calculation. The solar wind plasma and IMF data are

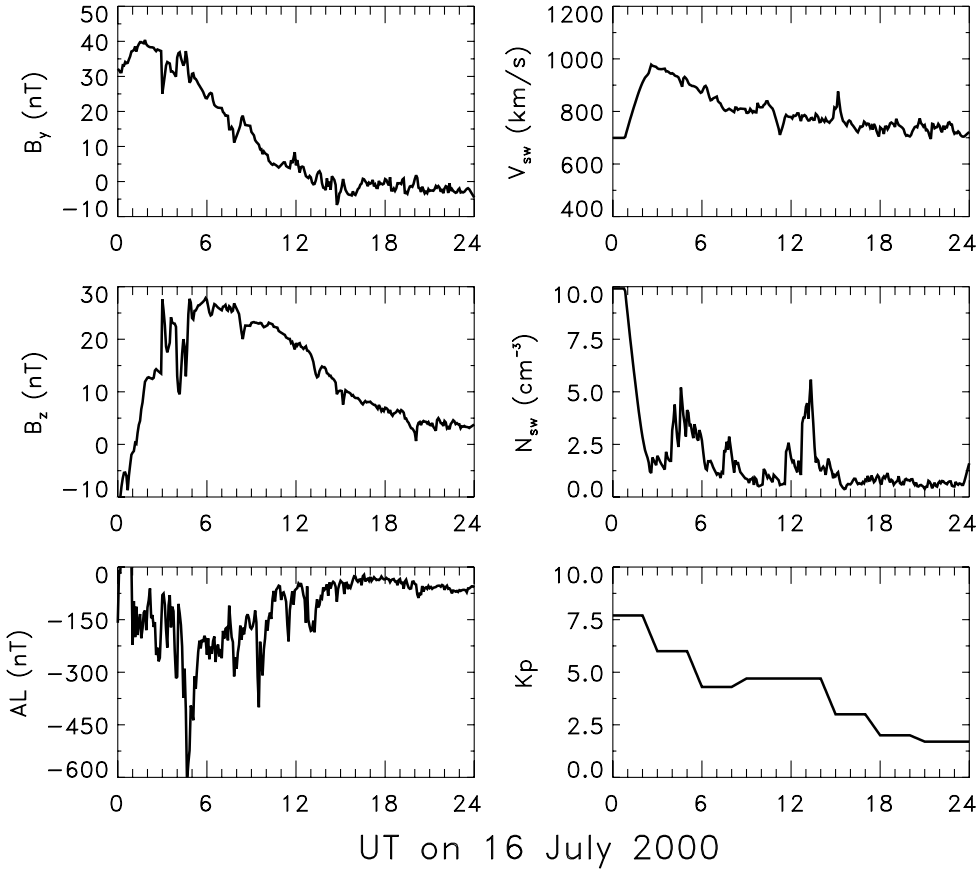

Figure 13. Some time-shifted solar wind and IMF parameters, and geomagnetic *AL* and K_p indices on 16 July 2000.

obtained from the ACE satellite and then shifted to the high-latitude ionospheric polar region using equation (4). It is noted that the time shift determined by equation (4) may have some errors, partially because the IMF structure is often tilted with respect to the Sun-Earth line [*Collier et al.*, 1998]. Therefore there may be a time shift between the outputs of the CEJH model and the results from AMIE.

[35] The potential drop and the Joule heating power are calculated from the CEJH model, taking input parameters from Figure 13. We also use AMIE to calculate the potential drop and the Joule heating power for the same day. The comparison of the outputs of our model with the results from AMIE is shown in Figure 14. The difference between our model results with (black solid line) and without (red dots) *AL* indices is quite small, and thus the effect of geomagnetic substorm on the potential drop during this storm is not significant as shown in the top panel. It is noted that "without *AL* index" means that we do not consider the effect of *AL* index on the potential drop in our calculation [*Weimer*, 2001]. The potential drop values calculated from our model are approximately consistent with those from AMIE except for the short period from 0200 UT to 0400 UT. Because the Weimer electric field model may not have a saturation function for large values of the solar wind speed and IMF magnitude [*Siscoe et al.*, 2002], this model overestimates the true polar cap potential during that period in which the solar wind plasma and IMF are highly disturbed as shown in Figure 13. Owing to the same reason, similar

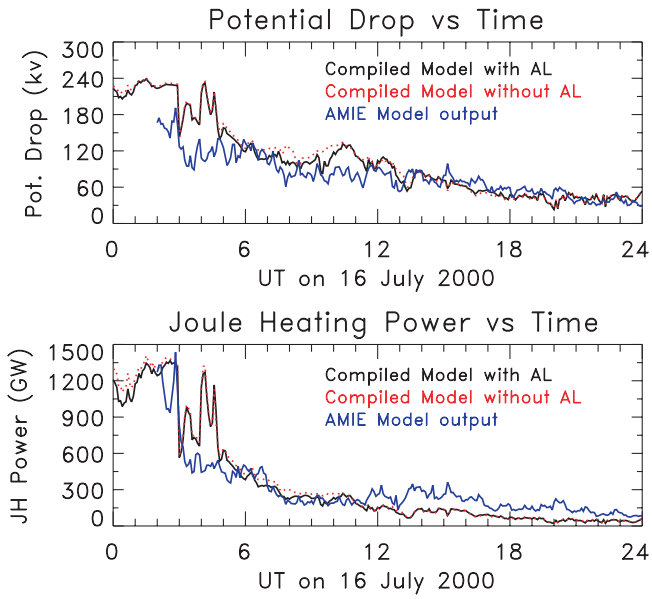

Figure 14. Comparison of the outputs of the compiled empirical model with the results from AMIE for the 16 July 2000 storm. The top panel is the polar potential comparison, and the bottom panel is the total Joule heating power comparison.

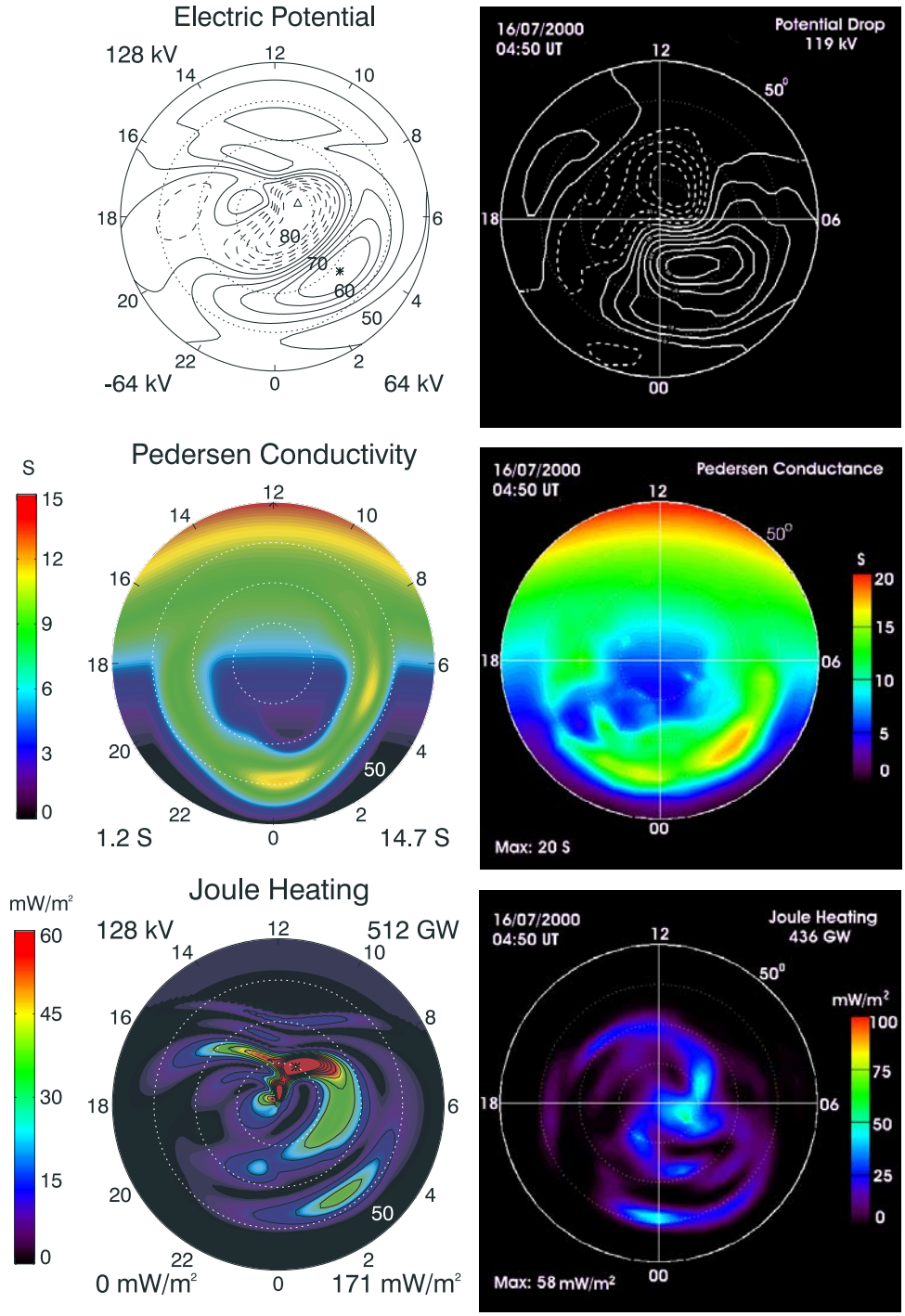

Figure 15. Snapshots of the outputs from the CEJH model (left) and AMIE (right) at 0450UT for the 16 July 2000 storm. (details in the text).

thing happens to the Joule heating power results, as shown in the bottom panel, and geomagnetic substorm does not significantly affect the Joule heating power for this storm. For highly disturbed solar wind conditions, our compiled empirical model produces higher Joule heating power than AMIE, whereas it gives lower Joule heating power than AMIE for less disturbed solar wind conditions. It is shown that the total Joule heating power calculated from our compiled empirical model is overall consistent with that from AMIE except for the short period with large solar wind speed and IMF magnitude.

[36] Figure 15 shows the snapshots of electric potentials (top panel), total Pedersen conductivities (middle panel), and Joule heating (bottom panel) obtained from the CEJH model (left column) and AMIE (right column) at 0450 UT for the 16 July 2000 storm, for the shifted solar wind and IMF input parameters, V_{sw} = 931 km/s, N_{sw} = 3.5 cm^{-3}, B_x = 5.0 nT, B_y = 28.2 nT, B_z = 27.7 nT, geophysical indices AL =

−523 nT and K_p = 6, and $F_{10.7}$ = 226. There is a 39-min propagation delay to 0450 UT.

[37] In the top panel, the positive and negative potentials are indicated by solid lines and dashed lines, respectively. The minimum potential (indicated with a triangle), −64 kV, the maximum potential (indicated with an asterisk), 64 kV, and the potential drop, 128 kV, are noted in the lower left, lower right, and upper left corner of the top left panel. The potential drop, 119 kV, is noted in the upper right corner of the top right panel. It is shown that the potential patterns resulting from the Weimer 2K model and AMIE are quite similar in large spatial scales, mainly with two convection cells. The potential drop from the Weimer 2K model is slightly higher than the potential drop from AMIE. These clockwise tilted potentials produce weak electric fields in the prenoon and premidnight regions. The middle panels display the total hight-integrated Pedersen conductivities from the Hardy model and the Rich model (left plot) and from AMIE (right plot). The maximum values of conductivities, 14.7 S and 20 S, are noted in the lower right corner of the left plot and in the lower left corner of the right plot. In order to compare the structures of these conductivity distributions, we use different color bars. The conductivities from the two models have similar structures except that there is a gap in the premidnight region at around 2000 UT. In the bottom panel, the distributions of the Joule heating from the CEJH model and AMIE show similar large-scale structures, which are confined to the same regions in the high-latitude ionosphere but also have different detailed features. The total Joule heating power, 512 GW, from the CEJH model is higher than the AMIE Joule heating power, 436 GW. Noted that different color bars are used in order to compare large-scale structures of the Joule heating distributions.

[38] We can see that results from the CEJH model and AMIE as shown in Figure 15 display similar large spatial structures but with different detailed features. However, we have to admit that these comparisons do not mean that the Joule heating rate and distribution resulting from the CEJH model are real or correct unless all submodels included in this compiled model are accurate and reliable. On the another hand, AMIE needs statistical conductance model to provide initial values for its run and the reliability of its outputs also depends on the validity and reliability of the statistical conductivity model [*Lu et al.*, 2001]. In addition, the current spatial resolution of AMIE significantly wipes away small-scale gradients associated with localized enhanced strong convection and plasma flows [*Lu et al.*, 2001]. Therefore the large-scale structures from the CEJH model have, as a first-order estimation, qualitatively consistent with the results from AMIE, but they have different detailed features.

5. Discussion and Summary

[39] It is noted that the CEJH model depends on certain electric potential, magnetic field, Pedersen conductivity, and neutral wind models. The CEJH model is based on the fact that its validity and effectiveness depend on the validity and effectiveness of its constructing models. That is why only the most robust and popular models are selected. The main purpose is to construct an empirical model to provide a quick and efficient way to evaluate global Joule heating input to the thermosphere, instead of developing complicated three-dimensional model to calculate Joule heating. If one model does not show its dependence on a particular parameter, it is either because there is no such strong dependence or because of the limitation of the model. For the former case, it is reasonable that the combined model dependence on particular parameters is driven by a certain submodel. Since the electric potential from the Weimer 2K model is directly driven by the solar wind/IMF parameters, it is natural that the Joule heating is also directly driven by them in our compiled model, even though some other parameters contributing to Joule heating are not directly driven by solar wind/IMF parameters, e.g., auroral particle precipitation and solar radio flux. However, as a first-order estimation, it is appropriate to use this model to study the global distribution of Joule heating and capture its basic behavior under different solar wind and IMF conditions, geomagnetic activities and solar EUV radiation conditions. For the later case, we need to use better submodels, when available, to replace the currently used submodels. Our compiled empirical model provides a very flexible infrastructure for such improvements. Even though the number of satellites and ground-based instruments has increased significantly over the past decades, data coverage is far from complete for developing fully functional empirical models. Thus it is required to plug better empirical models in the CEJH model when they are available:

[40] 1. The electric potential model in the CEJH model may need a saturation function to prevent overestimating the potential drop for large values of the solar wind speed and IMF because the Weimer 2K model dose not have a saturation function for large values of the solar wind speed and IMF magnitude. The electric field variation model might also be required [*Matsuo et al.*, 2003], since neglecting ionospheric electric field variations may cause calculation error of Joule heating on different temporal and spatial scales.

[41] 2. It is desirable that for higher altitude ionosphere, a more realistic geomagnetic field model, such as Tsygananko 2004 model, be included in the CEJH model. However, for low-altitude ionosphere, the IRGF model and the Tsyganako 1989 model should be appropriate to calculate the geomagnetic field in the CEJH model.

[42] 3. Hardy model uses a 3-hour K_p index and cannot reflect processes of much shorter timescales because a mixture of various solar wind/IMF conditions and substorm phases can occur within 3 hours (the typical timescale of auroral disturbances is minutes). Newly updated Pedersen conductivity models [*Zhang et al.*, 2004] from particle precipitation and from the solar radio flux are expected to be included in the CEJH model instead of *Hardy et al.* [1987] and *Rich et al.* [1987] models.

[43] 4. The neutral winds from the HWM93 model is of an average neutral winds. Since only midlatitude and low-latitude neutral winds can be predicted quite well by this model, we will also use the Thermosphere-Ionosphere Nested Grid (TING) model to calculate the neutral wind in the CEJH model, instead of the HWM 93 model. The TING model is a physics-based first-principal model that can perform high-resolution simulations in a specified local area, such as high-latitude regions [*Wang et al.*, 1999]. We will use observational data such as those from Fabry-Perot

Interferometers (FPI) measurements to evaluate neutral winds obtained from both the TING model and HWM93 and perform a more detailed study on the neutral wind effect on the energy deposition in the upper atmosphere during geomagnetic storms.

[44] As a demonstration, the CEJH model is used to study the dependence of the Joule heating pattern on the IMF clock angle, AL, K_p, and $F_{10.7}$ indices, other solar wind parameters such as B_T, V_{sw}, and N_{sw}, the Earth's dipole tilt, and the neutral wind. The results of the CEJH model help us understand the fundamental physical processes in the high-latitude ionosphere and upper atmosphere. The outputs of this model, such as the Joule heating power and the global Joule heating pattern, can be used by other models as inputs to examine large-scale energy deposition during disturbed geospace conditions and to describe the global structure and dynamic properties of the thermosphere and ionosphere. Below are what we find using our model in this study:

[45] 1. The CEJH model is constructed based on existing popular and robust empirical models, and as a first-order estimation, this model can be used to predict the Joule heating pattern, the Joule heating power, and the polar potential size in the high-latitude ionosphere and upper atmosphere.

[46] 2. It is found that the IMF orientation and its magnitude, the solar wind speed, AL index, K_p index, and $F_{10.7}$ index are important parameters to control the Joule heating pattern, the Joule heating power, and the polar potential size, as well as the effects of the neutral wind. Other parameters, such as N_{sw} and the Earth's dipole tilt, play less important roles for them.

[47] 3. The neutral wind could increase or reduce the Joule heating but it mainly depends on the IMF orientation and its magnitude, the solar wind speed [*Ridley et al.*, 2003; *Richmond et al.*, 2003], AL index, K_p index, and $F_{10.7}$ index. It is shown that the increase or reduction of the neutral wind contribution to Joule heating is not significant comparing with the convection Joule heating for less disturbed solar wind conditions, whereas under extreme solar wind conditions it can significantly contribute to Joule heating [*Lu et al.*, 1995; *Emery et al.*, 1999].

[48] 4. The results obtained from the CEJH model is basically consistent with those from AMIE. Because of the lack of a saturation function, our model gives higher values for the polar cap potential drop and the Joule heating power during highly disturbed solar wind conditions than AMIE, whereas it gives lower values for less disturbed solar wind conditions than AMIE.

[49] The CEJH model can be used as a complement to AMIE because of the following reasons: (1) AMIE depends on various data sets available, including the ion drift, auroral precipitation measurements and observations, and auroral UVI images from the DMSP F10, F12, and F13 satellites, the NOAA 12 and 14 satellites, the Polar satellite, six SuperDARN high-frequency radars, and the Millstone Hill and Sondrestrom incoherent scatter radar. It also depends on magnetic perturbation data from ground magnetometers [*Lu et al.*, 2001]. The locations of satellites and radars provide a limited geographical coverage. For example, SuperDARN covers 1800 MLT centered around the dusk-midnight sector. The CEJH model can be used to provide global coverage, especially to fill the gaps when there is no observed data available; (2) AMIE underestimates Joule heating during strong storms [*Chun et al.*, 1999]; and (3) AMIE currently does not include the effects of the thermospheric neutral winds [*Lu et al.*, 2001]. In addition, AMIE has been widely accepted as a research tool and still needs to improve data accessibility for space weather prediction. Even though the CEJH model gives higher values for the Joule heating power and potential drop during strong storm than AMIE, it does provide a quick and efficient way to predict the Joule heating power, the polar potential size, and the Joule heating patterns on global scales for space weather forecasting.

[50] It is noted that all input-driven parameters to the submodels are required to be available in advance when the CEJH model is used. Besides accessing solar wind and IMF data, it is necessary to develop an accurate method to estimate AL, K_p, or A_p indices using solar wind plasma and IMF data, since they are not independent of each other in the high-latitude polar region. It is also necessary to predict $F_{10.7}$ index. For example, $E_{10.7}$ is another solar radio flux agency that can be used as $F_{10.7}$ [*Tobiska et al.*, 2000]. After achieving these goals, it is possible to use the CEJH model to predict the global Joule heating patterns and the Joule heating power in the high-latitude ionosphere and upper atmosphere in the sense of space weather forecasting.

[51] The question might arise about how to justify why we use the CEJH model to predict the global Joule heating patterns, instead of using some complex three-dimensional models which should give better results for the basic properties. We have to realize that the Joule heating patterns from the CEJH model may be unreliable unless all submodels included in the CEJH model are accurate. One of the main purpose of the CEJH model is to provide a quick way to effectively and reasonably predict ionosphere Joule heating. This special purpose determines that we have to use some efficient empirical models in this study. The empirical models in the CEJH model have been widely used in the space physics community, just like many current publications using much simplified models, say dipole in some inner magnetosphere studies. More importantly, as a first-order estimation, the CEJH model helps understand the contributions of individual physical variations, as well as changes of Joule heating strength.

[52] **Acknowledgments.** We thank G. Lu for running AMIE for the 16 July 2000 storm and many helpful discussions. We also thank ACE SWEPAM and MFI teams and geomagnetic index teams for providing the data. We do appreciate D. R. Weimer, D. A. Hardy, F. J. Rich, N. A. Tsygenanko, and J. M. Quinn for providing the empirical models used in this study. This work was supported by grant NNSFC 40325010, Ministry of Science and Technology of China grant G2000078406, and also supported in part by the International Collaboration Research Team Program of the Chinese Academy of Sciences.

[53] Shadia Rifai Habbal thanks both referees for their assistance in evaluating this paper.

References

Ahn, B.-H., S.-I. Akasofu, and Y. Kamide (1983), The Joule heat production rate and the particle energy injection rate as a function of the geomagnetic indices *AE* and *AL*, *J. Geophys. Res.*, *88*, 6275–6287.

Ahn, B.-H., A. D. Richmond, Y. Kamide, H. W. Kroehl, B. A. Emery, O. De la Beaujardiere, and S.-I. Akasofu (1998), An ionospheric conductance model based on ground magnetic disturbance data, *J. Geophys. Res.*, *103*, 14,769–14,780.

Aksnes, A., J. Stadsnes, J. Bjordal, N. Tgaard, R. R. Vondrak, D. L. Detrick, T. J. Rosenberg, G. A. Germany, and D. Chenette (2002), Instantaneous ionospheric global conductance maps during an isolated substorm, *Ann. Geophys.*, *20*, 1181–1191.

Baker, J. B. H., Y. Zhang, R. A. Greenwald, L. J. Paxton, and D. Morrison (2004), Height-integrated Joule and auroral particle heating in the night side high latitude thermosphere, *Geophys. Res. Lett.*, *31*, L09807, doi:10.1029/2004GL019535.

Boyle, C. B., P. H. Reiff, and M. R. Hairston (1997), Empirical polar cap potentials, *J. Geophys. Res.*, *102*, 111–126.

Chao, J. K., D. J. Wu, C.-H. Lin, Y. H. Yang, X. Y. Wang, M. Kessel, S. H. Chen, and R. P. Lepping (2001), Models for the size and shape of the Earth's magnetopause and bow shock, paper presented at 2000 COSPAR Colloquium on Space Weather Study: Using Multi-Point Techniques, Comm. on Space Res., Wanli, Taipei.

Chun, F. K., D. J. Knipp, M. G. McHarg, G. Lu, B. A. Emery, S. Vennerstrom, and O. A. Troshichev (1999), Polar cap index as a proxy for hemispheric Joule heating, *Geophys. Res. Lett.*, *26*, 1101–1104.

Codrescu, M. V., T. J. Fuller-Rowell, and J. C. Foster (1995), On the importance of E-field variability for Joule heating in the high latitude thermosphere, *J. Geophys. Lett.*, *22*, 2393–2396.

Codrescu, M. V., T. J. Fuller-Rowell, J. C. Foster, J. M. Holt, and S. J. Cariglia (2000), Electric field variability associated with the Millstone Hill electric field model, *J. Geophys. Res.*, *105*, 5265–5274.

Collier, M. R., J. A. Slavin, R. P. Lepping, A. Szabo, and K. Ogilvie (1998), Timing accuracy for the simple planar propagation of magnetic field structures in the solar wind, *Geophys. Res. Lett.*, *25*, 2509–2512.

Crowley, G., and C. Hackert (2001), Quantification of high latitude electric field variability, *Geophys. Res. Lett.*, *28*, 2783–2786.

Deng, W., T. L. Killeen, A. G. Burns, R. M. Johnson, B. A. Emery, R. G. Roble, J. D. Winningham, and J. B. Gary (1995), One-dimensional hybrid satellite track model for the Dynamics Explorer 2 (DE 2) satellite, *J. Geophys. Res.*, *100*, 1161–1624.

Emery, B. A., C. Lathuillere, P. G. Richards, R. G. Roble, M. J. Buonsanto, D. J. Knipp, P. Wilkinson, D. P. Sipler, and R. Niciejewski (1999), Time dependent thermospheric neutral response to the 2–11 November 1993 storm period, *J. Atmos. Terr. Phys.*, *61*, 329–350.

Foster, J. C., J.-P. St.-Maurice, and V. J. Abreu (1983), Joule heating at high latitudes, *J. Geophys. Res.*, *88*, 4885–4896.

Fujii, R., S. Nozawa, and S. C. Buchert (1999), Statistical characteristics of electromagnetic energy transfer between the magnetosphere, the ionosphere and the thermosphere, *J. Geophys. Res.*, *104*, 2357–2365.

Gary, J. B., R. A. Heelis, W. B. Hanson, and J. A. Slavin (1994), Field aligned Poynting flux observations in the high latitude ionosphere, *J. Geophys. Res.*, *99*, 11,417–11,427.

Germany, G. A., D. G. Torr, P. G. Richards, M. R. Torr, and S. John (1994), Determination of ionospheric conductivities from FUV auroral emissions, *J. Geophys. Res.*, *99*, 23,297–23,305.

Gjerloev, J. W., and R. A. Hoffman (2000a), Height-intergrated conductivity in auroral substorms: 1. Data, *J. Geophys. Res.*, *105*, 215–226.

Gjerloev, J. W., and R. A. Hoffman (2000b), Height-intergrated conductivity in auroral substorms: 2. Modeling, *J. Geophys. Res.*, *105*, 227–235.

Hardy, D. A., M. S. Gussenhoven, and R. Raistrick (1987), Statistical and functional representations of the pattern of auroral energy flux, number flux, and conductivity, *J. Geophys. Res.*, *92*, 12,275–12,294.

Hedin, A. E., E. L. Fleming, A. H. Manson, F. J. Schmidlin, S. K. Avery, R. R. Clark, S. J. Franke, G. J. Fraser, T. Tsuda, F. Vial, and R. A. Vincent (1996), Empirical wind model for the upper, middle and lower atmosphere, *J. Atmos. Terr. Phys.*, *58*, 1421–1447.

Heppner, J. P., and N. C. Maynard (1987), Empirical high latitude electric field models, *J. Geophys. Res.*, *92*, 4467–4489.

Heppner, J. P., M. C. Liebrecht, N. C. Maynard, and R. F. Pfaff (1993), High latitude distributions of plasma waves and spatial irregularities from DE-2 alternating current electric field observations, *J. Geophys. Res.*, *98*, 1629–1652.

Liou, K., J. F. Carbary, P. T. Newell, C.-I. Meng, and O. Rasmussen (2003), Correlation of auroral power with the polar cap index, *J. Geophys. Res.*, *108*(A3), 1108, doi:10.1029/2002JA009556.

Lu, G., P. H. Rieff, M. R. Hairston, R. A. Heelis, and J. L. Karty (1989), Distribution of convection potential around the polar cap boundary as a function of the interplanetary magnetic field, *J. Geophys. Res.*, *94*, 13,447–13,461.

Lu, G., A. D. Richmond, B. A. Emery, and R. G. Roble (1995), Magnetosphere-ionosphere-thermosphere coupling: Effect of neutral winds on energy transfer and field-aligned current, *J. Geophys. Res.*, *100*, 19,643–19,659.

Lu, G., A. D. Richmond, J. M. Ruohoniemi, R. A. Greenwald, M. Hairston, F. J. Rich, and D. S. Evans (2001), An investigation of the influence of data and model inputs on assimilative mapping of ionospheric electrodynamics, *J. Geophys. Res.*, *106*, 417–434.

Matsuo, T., A. D. Richmond, and K. Hensel (2003), High latitude ionospheric electric field variability and electric potential derived from DE-2 plasma drift measurements: Dependence on IMF and dipole tilt, *J. Geophys. Res.*, *108*(A1), 1005, doi:10.1029/2002JA009429.

Olsson, A., P. Janhunen, T. Karlsson, N. Ivchenko, and L. G. Blomber (2004), Statistics of Joule heating in the auroral zone and polar cap using Astrid-2 satellite Poynting flux, *Ann. Geophys.*, *22*, 4133–4142.

Palmroth, M., P. Janhunen, T. I. Pulkkinen, and H. E. J. Koskinen (2004), Ionospheric energy inputs as a function of solar wind parameters: Global MHD simulation results, *Ann. Geophys.*, *22*, 549–566.

Papitashvili, V. O., B. A. Belov, D. S. Faermark, Y. I. Feldstein, S. A. Golyshev, L. I. Gromova, and A. E. Levitin (1994), Electric potential patterns in the northern and southern polar regions parameterized by the interplanetary magnetic field, *J. Geophys. Res.*, *99*, 13,251–13,262.

Papitashvili, V. O., F. J. Rich, M. A. Heinemann, and M. R. Hairston (1999), Parameterization of the Defense Meteorological Satellite Program ionospheric electrostatic potentials by the interplanetary magnetic field strength and direction, *J. Geophys. Res.*, *104*, 177–184.

Rich, F. J., and M. Hairston (1994), Large-scale convection patterns observed by DMSP, *J. Geophys. Res.*, *99*, 3827–3844.

Rich, F. J., M. S. Gusshoven, and M. E. Greenspan (1987), Using simultaneous particle and field observations on a low altitude satellite to estimate Joule heating energy flow into the high latitude ionosphere, *Ann. Geophys.*, *5A*, 527–534.

Richmond, A. D., and Y. Kamide (1988), Mapping electrodynamic features of the high latitude ionosphere from localized observation: Technique, *J. Geophys. Res.*, *93*, 5741–5759.

Richmond, A. D., C. Lathuille're, and S. Vennerstroem (2003), Winds in the high latitude lower thermosphere: Dependence on the interplanetary magnetic field, *J. Geophys. Res.*, *108*(A2), 1066, doi:10.1029/2002JA009493.

Ridley, A. J., G. Crowley, and C. Freitas (2000), An empirical model of the ionospheric electric potential, *Geophys. Res. Lett.*, *27*, 3675–3678.

Ridley, A. J., A. D. Richmond, T. I. Gombosi, D. L. De Zeeuw, and C. R. Clauer (2003), Ionospheric control of the magnetospheric configuration: Thermospheric neutral winds, *J. Geophys. Res.*, *108*(A8), 1328, doi:10.1029/2002JA009464.

Ruohoniemi, J. M., and R. A. Greenwald (1996), Statistical patterns of high latitude convection obtained from Goose Bay HF radar observations, *J. Geophys. Res.*, *101*, 21,743–21,764.

Semeter, J., and R. Doe (2002), On the proper interpretation of ionospheric conductance estimated through satellite photometry, *J. Geophys. Res.*, *107*(A8), 1200, doi:10.1029/2001JA009101.

Shepherd, S. G., R. A. Greenwald, and J. M. Ruohoniemi (2002), Cross polar cap potentials measured with Super Dual Auroral Radar Network during quasi-steady solar wind and interplanetary magnetic field conditions, *J. Geophys. Res.*, *107*(A7), 1094, doi:10.1029/2001JA000152.

Siscoe, G. L., G. M. Erickson, B. U. Ö. Sonnerup, N. C. Maynard, J. A. Schoendorf, K. D. Siebert, D. R. Weimer, W. W. White, and G. R. Wilson (2002), Hill model of transpolar potential saturation: Comparisons with MHD simulations, *J. Geophys. Res.*, *107*(A6), 1075, doi:10.1029/2001JA000109.

Spiro, R. W., P. H. Reiff, and L. J. Maher Jr. (1982), Precipitating electron energy flux and auroral zone conductance: An empirical model, *J. Geophys. Res.*, *87*, 8215–8227.

Thayer, J. P., J. F. Vickrey, R. A. Heelis, and J. B. Gary (1995), Interpretation and modeling of the high latitude electromagnetic energy flux, *J. Geophys. Res.*, *100*, 19,715–19,728.

Tobiska, W. K., T. Woods, and F. Eparvier, et al. (2000), The SOALR2000 empirical solar irradiance model and forecast tool, *J. Atmos. Sol. Terr. Phys.*, *62*, 1233–1250.

Tsyganenko, N. A. (1989), A magnetospheric magnetic field model with wraped tail current sheet, *Planet. Space Sci.*, *37*, 5–20.

Wang, W., T. L. Killeen, A. G. Burns, and R. G. Roble (1999), A high resolution, three-dimensional, time dependent, nested grid model of the coupled thermosphere-ionosphere, *J. Atmos. Sol. Terr. Phys.*, *61*, 385–397.

Wang, W., M. Wiltberger, A. G. Burns, S. C. Solomon, T. L. Killeen, N. Maruyama, and J. G. Lyon (2004), Initial results from the coupled magnetosphere-ionosphere-thermosphere model: Thermosphere-ionosphere responses, *J. Atmos. Sol. Terr. Phys.*, *66*, 1425–1441.

Weimer, D. R. (1995), Models of high latitude electric potentials derived with a least error fit of spherical harmonic coefficients, *J. Geophys. Res.*, *100*, 19,595–19,608.

Weimer, D. R. (2001), An improved model of high latitude ionospheric electric potentials having "space weather" application, *J. Geophys. Res.*, *106*, 407–416.

Zhang, B.-C., Y. Kamide, R.-Y. Liu, H. Shinagawa, and K. Iwamasa (2004), A modeling study of ionospheric conductivities in the high latitude electrojet regions, *J. Geophys. Res.*, *109*, A04310, doi:10.1029/2003JA010181.

T. Chen and C. Wang, Key Laboratory of Space Weather, Center for Space Science and Applied Research, Chinese Academy of Sciences, 100080 Beijing, China. (tchen@center.cssar.ac.cn; cw@spaceweather.ac.cn)

G. A. Germany and T. S. Wu, Center for Space Plasma and Aeronomic Research, University of Alabama in Huntsville, Huntsville, AL 35899, USA. (germanyg@cspar.uah.edu; wus@cspar.uah.edu)

A. Tan, Physics Department, Alabama A. & M. University, Normal, AL 35762, USA. (arjun.tan@email.aamu.edu)

W. Wang, High Altitude Observatory, National Center for Atmospheric Research, Boulder, CO 80307, USA. (wbwang@hao.ucar.edu)

Y. L. Wang, Space Science and Applications, Los Alamos National Laboratory, Los Alamos, NM 87545, USA. (ywang@lanl.gov)

X. X. Zhang, Physics Department, Auburn University, 206 Allison Laboratory, Auburn, AL 36849, USA. (xxzhang@physics.auburn.edu)